Inorganic Chemistry

pubs.acs.org/IC Article

Toward Frameworks with Multiple Aligned and Interactive $Fe(CO)_3$ Rotators: Syntheses and Structures of Diiron Complexes Linked by Two *trans*-Diaxial α,ω-Diphosphine Ligands $Ar_2P(CH_2)_nPAr_2$

Samuel R. Zarcone, Gong M. Chu, Andreas Ehnbom, Ashley Cardenal, Tobias Fiedler, Nattamai Bhuvanesh, Michael B. Hall,* and John A. Gladysz*

Cite This: *Inorg. Chem.* 2021, 60, 3314−3330

ABSTRACT: Reactions of (η^4-benzylideneacetone)$Fe(CO)_3$ and the α,ω-diphosphines $Ar_2P(CH_2)_nPAr_2$ afford the trigonal bipyramidal diiron tetraphosphorus complexes *trans,trans*-$(CO)_3Fe[Ar_2P(CH_2)_nPAr_2]_2Fe(CO)_3$ (n/Ar = 3/Ph **3**, 4/Ph **4a**, 4/*p*-tol **4b**; 56−19%). Crystal structures establish essentially parallel P−Fe−P axes, iron−iron distances of 5.894(9)−5.782(1) Å (**3**) and 6.403(1)−6.466(1) Å (**4a,b**), and van der Waals radii of 4.45 Å for the $Fe(CO)_3$ rotators, the planes of which are offset by 0.029−1.665 Å. Analogous reactions of $Ph_2P(CH_2)_6PPh_2$ yield the square pyramidal monoiron complex *trans*-$(CO)_3\overline{Fe[Ph_2P(CH_2)_6PPh_2]}$ (**6′**, 31%), a rare case where a diphosphine spans *trans* basal positions (∠P−Fe−P 147.4(2)°). Both **3** and **6′** exhibit two CO ^{13}C NMR signals at room temperature, indicating slow exchange on the NMR time scale, which in the former could entail $Fe(CO)_3/Fe(CO)_3$ gearing. Under analogous conditions, **4a**,**b** exhibit one signal. Previously reported adducts of $Fe(CO)_3$ and $Ph_2P(CH_2)_nPPh_2$ are surveyed (1:1, n = 1−5; 2:2, n = 5), and the IR $\nu_{C\equiv O}$ band patterns and energies of all complexes analyzed with the aid of DFT calculations. The diiron complexes are preferred thermodynamically. Attention is given to limiting types of $Fe(CO)_3/Fe(CO)_3$ interactions in the diiron complexes.

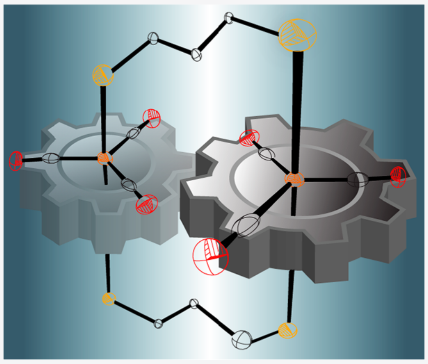

INTRODUCTION

There has been much recent interest in molecular rotors, a broad class of compounds that can be dissected into two components, rotators and stators.[1] In particular, assemblies with multiple rotators that are capable of coupled interactions hold promise for various types of molecular machines.[2−4] Such phenomena have been most intensively studied in the context of sterically driven gearing.[2,3] Purely electronic rotator/rotator interactions have also received attention.[4]

We have been engaged in the synthesis of what we term gyroscope like transition metal complexes.[5−8] These are most commonly accessed as shown in Scheme 1 (top). Complexes with two *trans*-trialkylphosphine ligands of the formula $P((CH_2)_mCH{=}CH_2)_3$ (**I**) are first prepared. Then 3-fold intramolecular ring closing alkene metatheses are carried out. Subsequent hydrogenations afford target complexes **II** with triply *trans*-spanning dibridgehead diphosphine ligands in surprisingly high overall yields. Depending upon the sizes of the ligands on the metal (L_y) and the lengths of the $(CH_2)_n$ segments ($n = 2m + 2$), the ML_y moieties in **II** may (or may not) be able to rotate within the cage like diphosphine.[5−8]

As sketched in Scheme 1 (bottom), we sought to extend this effort to related bimetallic complexes with sterically coupled ML_y rotators, both with (**IV**) and without (**III**) protective *trans*-spanning polyphosphine ligands. A significant portion of our results with **II** have involved trigonal bipyramidal iron complexes with the rotators $Fe(CO)_3$, $Fe(CO)_2(NO)^+$, and $Fe(CO)(NO)(X)$ (X = Cl, Br, I, and CN).[7] Hence, for initial exploratory studies, a minimalist approach involving reactions of α,ω-diphosphines $Ar_2P(CH_2)_nPAr_2$ and $Fe(CO)_3$ sources was selected, as outlined in Scheme 2. We were particularly interested in accessing diiron tetraphosphorus species **V** with n = 3 and 4. For these systems, molecular models suggested sterically interactive rotators. Indeed, as described below, this simple strategy does afford the target complexes.

During the later stages of this work, we became aware of a similar synthesis of species **V** with n/Ar = 5/Ph by Liu and Gau.[9] Furthermore, as shown in Scheme 2, reactions of diphosphines $Ar_2P(CH_2)_nPAr_2$ and $Fe(CO)_3$ sources are also capable, in principle, of giving monoiron diphosphorus species such as **VI**, as well as oligomers or other adducts. Indeed, there are several previous reports of **VI** (Ar = Ph) with n ranging from 1 to 5.[10−14] As outlined below, these can exhibit different

Received: December 21, 2020
Published: February 11, 2021

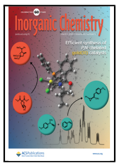

Scheme 1. Syntheses of Gyroscope-Like Complexes (II) and New Targets with Two ML_y Rotators with Parallel Axes (III and IV)

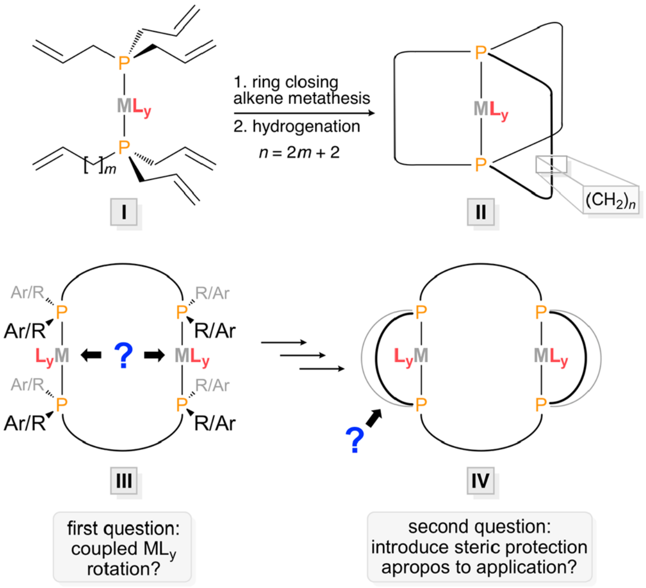

Scheme 2. Some Possible Products Derived from Equimolar Amounts of $Fe(CO)_3$ Sources and α,ω-Diphosphines $Ar_2P(CH_2)_nPAr_2$ (V and VI)

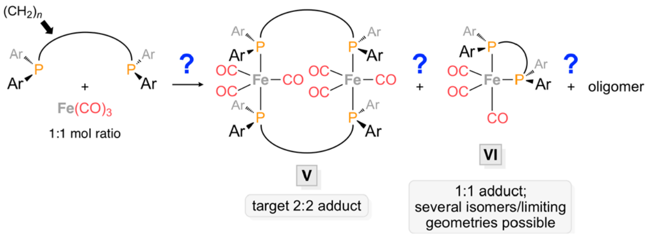

Scheme 3. Syntheses of New Diiron and Monoiron Complexes

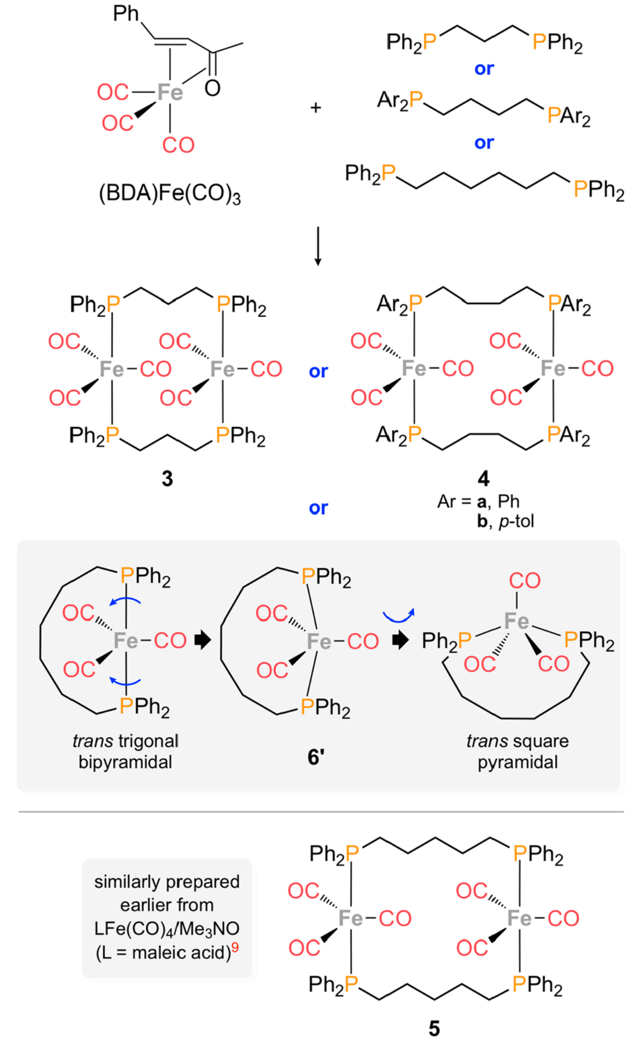

limiting geometries,[11] and as a collateral result of this study, a rare type of isomer has been isolated in the case of $n = 6$. To provide additional support for the structural assignments made herein and in earlier reports,[9−14] as well as a road map to guide future research, the IR $\nu_{C\equiv O}$ patterns are computed by DFT methods and compared to those found experimentally. These calculations furthermore yield free energies that show the equilibria 2**VI** ⇌ **V** to be exergonic.

■ RESULTS

Syntheses of Title Complexes. The η^4-benzylideneacetone complex $(BDA)Fe(CO)_3$[15] has seen extensive use as a functional equivalent of the $Fe(CO)_3$ fragment.[7a,15,16] The phenyl substituted α,ω-diphosphines $Ph_2P(CH_2)_nPPh_2$ ($n = 3$, 4, and 6) were obtained from commercial sources, and the *p*-tolyl analog $(p\text{-tol})_2P(CH_2)_4P(p\text{-tol})_2$ was isolated in 47% yield from the reaction of the phosphido anion $(p\text{-tol})_2P^-\ Li^+$ and the corresponding α,ω-dibromide. This 1,4-diphosphine had been previously synthesized from $Cl_2P(CH_2)_4PCl_2$ and the Grignard reagent *p*-tolMgBr.[17]

Accordingly, $(BDA)Fe(CO)_3$ was treated with 1.2 equiv of $Ph_2P(CH_2)_3PPh_2$ (1,3-bis(diphenylphosphino)propane) or $Ph_2P(CH_2)_4PPh_2$ (1,4-bis(diphenylphosphino)butane) in THF. After 48 h, the solvent was removed. As shown in Scheme 3, workups gave the target complexes *trans,trans*-$(CO)_3Fe[Ph_2P(CH_2)_nPPh_2]_2Fe(CO)_3$ ($n = 3$ (**3**) and 4 (**4a**)) as air-sensitive yellow or pale yellow solids in 44 and 19% yields, respectively.

These and all other new complexes below were characterized by microanalyses, IR spectroscopy (ATR and powder film) and NMR spectroscopy (^1H, $^{13}C\{^1H\}$, and $^{31}P\{^1H\}$). The IR $\nu_{C\equiv O}$ bands are depicted in Figure 1 and summarized in Table 1. The remaining data are given in the Experimental Section. Both **3** and **4a** were soluble in toluene, THF, and DMSO and insoluble in hexane. Although **3** was insoluble in CH_2Cl_2, **4a** was soluble in both CH_2Cl_2 and $CDCl_3$.

The spectroscopic properties of **3** and **4a** were consistent with the proposed structures. In particular, the IR spectra showed one strong $\nu_{C\equiv O}$ band (1871 or 1864 cm^{-1}), and a second much weaker band at higher frequency (1969 or 1964 cm^{-1}). As can be derived from group theory,[18] this pattern is characteristic of axially disubstituted trigonal bipyramidal complexes of the formula *trans*-$Fe(CO)_3L_2$. However, there are many literature reports (L = phosphine) in which the weaker band is missing or has possibly been overlooked.[7a,16b] This includes the higher homologue derived from 1,5-bis(diphenylphosphino)pentane, *trans,trans*-$(CO)_3Fe[Ph_2P(CH_2)_5PPh_2]_2Fe(CO)_3$ (**5**; 1877 cm^{-1}),[9] which is depicted in Scheme 3 (bottom; see the Introduction).[19]

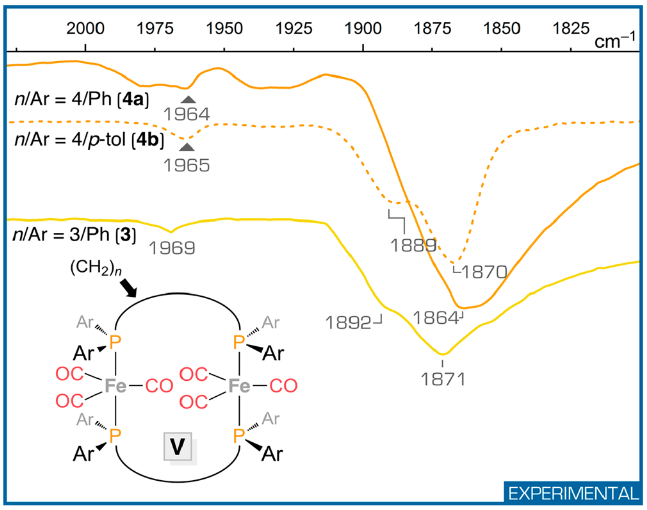

Figure 1. IR spectra (ATR/powder film, $\nu_{C\equiv O}$ region) of the new diiron complexes **V** with principal features highlighted.

Of course, the diiron complexes **3** and **4a** and the trigonal bipyramidal monoiron complexes *trans*-$Fe(CO)_3L_2$ have different molecular symmetries, and this will affect the vibrational spectra. Also, a shoulder was evident on the strong $\nu_{C\equiv O}$ band of **3** (1892 cm^{-1}; Figure 1). Thus, the IR $\nu_{C\equiv O}$ bands of all iron carbonyl complexes prepared or discussed in this paper have been computed using DFT, as summarized in Table 1 and described and analyzed below.

The NMR spectra also supported the structures of **3** and **4a**. With **3**, two CO $^{13}C\{^1H\}$ signals could be observed (214.7 and 212.4 ppm, both apparent m), consistent with sterically restricted $Fe(CO)_3$ rotators. To our knowledge, all monoiron diphosphorus adducts **VI** (Scheme 2) examined to date afford a single CO signal at ambient probe temperatures. In the case of **4a**, only a very weak CO signal (214.0 ppm) could be tentatively assigned. The $^{31}P\{^1H\}$ NMR chemical shifts of **3** and **4a** (75.12 and 73.96 ppm in DMSO-d_6) were also quite close to that of the analogous $Ph_2P(CH_2)_5PPh_2$ adduct **5** (75.53 ppm in $CDCl_3$).[9] The signal of the corresponding monoiron adduct *cis*-$(CO)_3Fe[Ph_2P(CH_2)_5PPh_2]$ (**5′**)[20] is much further upfield (55.46 ppm).

The preceding reactions were extended in two ways. First, with the idea of procuring more soluble complexes with additional NMR "handles", $(BDA)Fe(CO)_3$ was similarly combined with the *p*-tolyl substituted diphosphine $(p\text{-tol})_2P(CH_2)_4P(p\text{-tol})_2$ (0.8 equiv; Scheme 3). Workup gave the target complex *trans,trans*-$(CO)_3Fe[(p\text{-tol})_2P(CH_2)_4P(p\text{-tol})_2]_2Fe(CO)_3$ (**4b**) in 56% yield, which was soluble in the same solvents as **4a** and partially soluble in hexane. The IR spectrum showed two main $\nu_{C\equiv O}$ bands analogous to those of **3** and **4a** (1870 s and 1965 w cm^{-1}), and a shoulder as noted with **3** (1889 cm^{-1}; Figure 1 and Table 1). A high-resolution mass spectrum (ESI) gave an envelope of intense ions with the masses and isotope distribution expected for **4b** + H. The $^{13}C\{^1H\}$ NMR spectrum also showed a single CO signal that was coupled to phosphorus (220.7 ppm, t, J_{CP} = 8.7 Hz), consistent with rapid $Fe(CO)_3$ rotation on the NMR time scale. Although ^1H NMR spectra suggested a purity of ca. 90%, a crystalline sample was easily obtained as described below.

Second, $(BDA)Fe(CO)_3$ was similarly combined with the hexamethylene diphosphine $Ph_2P(CH_2)_6PPh_2$ (1.2 equiv) in THF (Scheme 3). A chromatographic workup of the red solution gave a yellow solid (31%) that was initially thought to be the diiron complex *trans,trans*-$(CO)_3Fe[Ph_2P(CH_2)_6PPh_2]_2Fe(CO)_3$ (**6**). However, a high-resolution mass spectrum (ESI) suggested a monoiron diphosphorus species. The IR spectrum showed a strong $\nu_{C\equiv O}$ band at 1863 cm^{-1} and a second weak one at 1965 cm^{-1}. Also, the $^{13}C\{^1H\}$ NMR spectrum exhibited two CO signals (ca. 2:1). These data were best reconciled with the structural assignment *trans*-$(CO)_3Fe[Ph_2P(CH_2)_6PPh_2]$ (**6′**),[20] as further supported in the following section.

Table 1. Experimental and Computed IR $\nu_{C\equiv O}$ Bands for Monoiron (1′−6′) and Diiron (3, 4a,b, 5, and 6) Complexes

complex	*n*	geometry[a]	$\nu_{C\equiv O}$ (cm^{-1}) experimental	medium	$\nu_{C\equiv O}$ (cm^{-1}) computed[b]
1′[c]	1	sq pyr *cis*[d]	1984 s, 1911 m, 1901 s	CH_2Cl_2	1968 s, 1915 s, 1911 s
2′[e]	2	sq pyr *cis*[d]	1982 s, 1913 m, 1892 s	CH_2Cl_2	1970 s, 1919 m, 1901 s
3′[f]	3	tbp *cis*	1982 s, 1909 m, 1881 s	CH_2Cl_2	1969 s, 1910 m, 1890 s
4′a[g]	4	tbp *cis*	1981 s, 1908 m, 1879 s	CH_2Cl_2	1966 s, 1907 m, 1882 s
4′b[h]	4	tbp *cis*			1964 s, 1904 m, 1880 s
5′[i]	5	tbp *cis*	1983 s, 1912 s, 1883 s	CH_2Cl_2	1964 s, 1906 m, 1882 s
6′[j]	6	sq pyr *trans*	1965 w, 1863 s	powder film	1941 w,[k] 1892 m, 1865 s
3[j]	3	tbp *trans*	1969 w, 1892 sh, 1871 s	powder film	1939 w,[k] 1889 sh, 1876 s
4a[j]	4	tbp *trans*	1964 w, 1864 s	powder film	1933 w,[k] 1871 sh, 1867 s
4b[j]	4	tbp *trans*	1965 w, 1889 sh, 1870 s	powder film	1930 w,[k] 1871 sh, 1862 s
5[i]	5	tbp *trans*	1877 s	CH_2Cl_2	1935 w,[k] 1873 sh, 1865 s
6[h]	6	tbp *trans*			1960 w,[k] 1897 s, 1893 s

[a] These correspond to the crystal structures for **1′**−**3′**, **5′**, **6′**, **3**, **4a,b**, and **5** and are replicated by the computed structures in all cases. [b] Determined by DFT as described in the text. [c] The experimental values are from ref 14b; similar data have been reported in refs 14a (1989 s, 1919 ms, 1909 s; $CHCl_3$) and 14c (1989, 1913, 1907; THF, no intensity information). [d] These complexes exhibit intermediate sq pyr/tbp geometries but are considered predominantly sq pyr; see refs 10−12. [e] The experimental values are from ref 14b; similar data have been reported in ref 14c (1984, 1914, 1888; THF, no intensity information). [f] The experimental values are from ref 14b; similar data have been reported in refs 13 (1983 s, 1908 ms, 1882 s; CH_2Cl_2/0.1 M Bu_4NPF_6), 14c (1984, 1914, 1888; THF, no intensity information), and 14d (1986 s, 1914 ms, 1984 vs; CH_2Cl_2 or 1980 s, 1908 s, 1885 vs; Nujol). [g] The experimental values are from ref 14b; similar data have been reported in ref 14c (1983, 1912, 1886; THF, no intensity information). This complex has not been crystallographically characterized. [h] This complex has not yet been synthesized. [i] The experimental values are from ref 9. [j] This work. [k] These absorptions are predicted to be very weak or undetectable.

The isolation of **6′** prompted us to check whether related monoiron species (**3′**, **4′a**, and **4′b**) might have been generated under the conditions used to access **3** and **4a,b**. As further detailed in the Experimental Section, species with plausible $^{31}P\{^1H\}$ NMR chemical shifts for such adducts were sometimes observed in the crude reaction mixtures but were

Table 2. General Crystallographic Data

	$3\cdot(CH_2Cl_2)_4$	$4a\cdot$(toluene)$_6$	4b[a]	$6'\cdot$(toluene)$_{0.5}$
empirical formula	$C_{64}H_{60}Cl_8Fe_2O_6P_4$	$C_{104}H_{104}Fe_2O_6P_4$	$C_{70}H_{72}Fe_2O_6P_4$	$C_{36.5}H_{36}FeO_3P_2$
formula weight	1444.30	1685.45	1244.86	640.44
temperature [K]	110(2)	110(2)	110(2)	120(2)
diffractometer	Bruker Gadds	Bruker Gadds	Bruker Quest	Bruker Quest
wavelength [Å]	1.5418	1.5418	0.71073	0.71073
crystal system	triclinic	triclinic	monoclinic	monoclinic
space group	$P\overline{1}$	$P\overline{1}$	$P2_1/c$	$P2_1/n$
unit cell dimensions				
a [Å]	12.5070(5)	11.2478(5)	12.2470(16)	10.1433(5)
b [Å]	12.5333(5)	15.2495(6)	15.299(2)	29.2030(14)
c [Å]	22.0792(8)	26.8362(12)	22.763(3)	10.7720(5)
α [deg]	88.807(3)	106.296(3)	90	90
β [deg]	73.868(2)	99.572(3)	94.774(2)	92.699(10)
γ [deg]	77.784(2)	94.533(3)	90	90
V [Å^3]	3246.8(2)	3246.8(2)	4250.2(10)	3187.3(3)
Z	2	2	2	4
ρ calc [Mg/m^3]	1.477	1.296	0.973	1.335
μ [mm^{-1}]	7.950	3.833	0.455	0.609
F(000)	1480	1776	1304	1340
crystal size [mm^3]	0.11 × 0.07 × 0.04	0.05 × 0.04 × 0.02	0.10 × 0.08 × 0.05	0.20 × 0.18 × 0.11
Θ limit [deg]	2.08−60.00	1.749−60.968	2.261−22.545	2.790−28.428
index range (h, k, l)	−13, 14; −4, 14; −24, 24	−12, 12; −17, 17; −30, 30	−13, 13; −16, 16; −24, 24	−13, 13; −39, 38; −14, 14
reflections collected	76986	92070	60697	43668
independent reflections	9463 [R(int) = 0.0701]	12925 [R(int) = 0.0701]	5547 [R(int) = 0.0488]	7998 [R(int) = 0.0372]
max. and min. transmission	0.7416 and 0.4751	0.7227 and 0.5462	0.4267 and 0.3776	0.4311 and 0.3852
data/restraints/parameters	9463/3/765	12925/346/976	5547/0/374	7998/456/481
goodness-of-fit on F^2	1.031	1.106	1.074	1.120
final R indices [$I > 2\sigma(I)$]				
R_1	0.0606	0.0945	0.0998	0.0331
wR_2	0.1508	0.1772	0.2644	0.0674
R indices (all data)				
R_1	0.0691	0.1262	0.1055	0.0470
wR_2	0.1563	0.1937	0.2683	0.0766
largest diff. peak/hole [e Å^{-3}]	1.881 and −1.073	0.707 and −0.675	1.025 and −0.661	0.397 and −0.342

[a] The crystal contained disordered solvent molecules, which were treated as described in the Experimental Section. As a result, the density is underestimated.

removed upon the prescribed workup. When concentrations were varied, these sometimes became the major products.

Structural Data. Crystals of solvates of **3**, **4a**, **4b**, and **6′** could be grown, and the X-ray structures were determined as outlined in Table 2 and the Experimental Section. Thermal ellipsoid plots are depicted in Figures 2 and 3. Key metrical parameters are listed in Tables 3 and 4. The latter emphasizes features relevant to nonbonded interactions in the diiron complexes, and includes the previously published structure for **5**[9] and DFT results for **6** described below. These two structures are depicted in Figure 4. For all complexes, the atoms have been renumbered from those in the CCDC files to achieve a uniform pattern that facilitates data comparison.

For both **3** and **4a**, two independent molecules were found in the unit cell, each with an inversion center. These are denoted as **3**(1), **3**(2), **4a**(1), and **4a**(2) in the graphics and tables. The structure of **4b** also exhibits an inversion center, and **5** features a C_2 axis that is perpendicular to the Fe_2P_4 plane. The radii of the $Fe(CO)_3$ rotators fall into a narrow range centered at 4.45 Å (Table 4), as computed by taking the average iron−oxygen distance and adding the van der Waals radius of an oxygen atom (1.52 Å).[21] Unsurprisingly, these closely agree with values found earlier.[7a]

Measures of the relationships between the two P−Fe−P axes of the diiron complexes were sought. Three nearly collinear points, each with independent experimental error, do not very accurately define a plane. Thus, least-squares planes derived from each P−Fe−P axis and the distal iron atom were calculated (P−Fe−P/Fe′). As summarized in Table 4, the complexes with inversion centers (**3** and **4a**,**b**) gave plane/plane angles of 0°, indicating rigorously parallel axes. The others (**5** and **6**) gave plane/plane angles of 7.6−12.0°. The relationships between the axes are also reflected by the four P−Fe−Fe′−P torsion angles, which as noted in Table 4 are always close to 0° or ±180°.

Measures of the relationships between the planes of the rotators were also sought. For this purpose, the four-atom least-squares $Fe(C)_3$ planes were used (as opposed to the seven-atom $Fe(CO)_3$ planes). The inversion centers in **3** and **4a**,**b** render the two $Fe(C)_3$ planes as parallel, so it is a simple matter to measure the offsets. In both independent molecules of **3**, the two planes are nearly coplanar (miniscule offsets of 0.087 and 0.029 Å). In the two independent molecules of **4a**, the separations increase significantly and are more highly differentiated (0.985 and 1.217 Å). In **4b**, the offset further

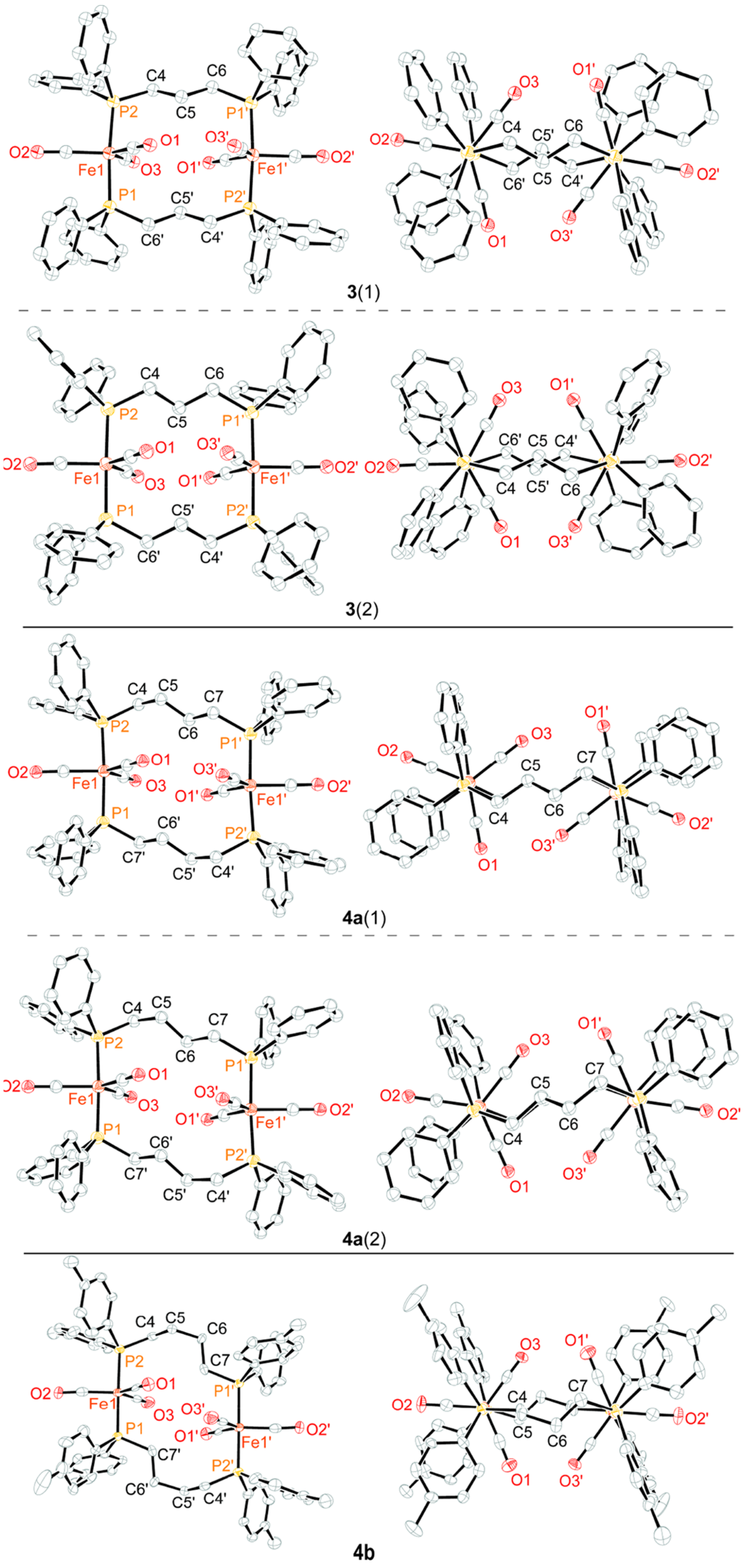

Figure 2. Thermal ellipsoid plots (50% probability) of the molecular structures of **3** (two independent molecules (1 and 2)), **4a** (two independent molecules (1 and 2)), and **4b**. Solvent molecules in the lattices have been omitted.

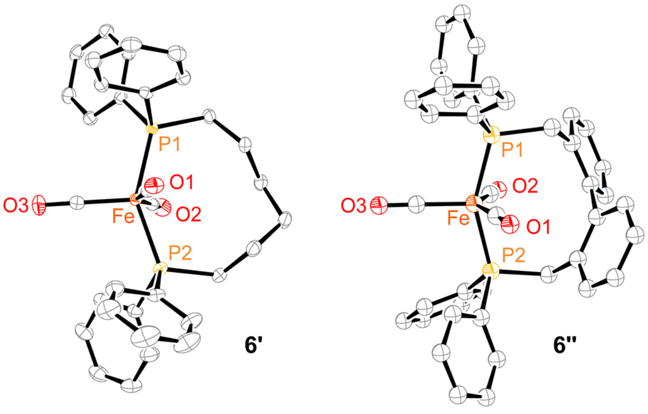

Figure 3. Thermal ellipsoid plots (50% probability) of the molecular structure of **6′** (left) and a relevant complex from the literature, **6″** (right; see the Discussion). Solvent molecules in the lattices have been omitted.

increases (1.677 Å). These relationships are illustrated in Figure 5.

In **5** and **6**, the Fe(C)$_3$ planes are no longer parallel; therefore, the rotators do not have a uniform separation. We have not been able to devise a meaningful geometric parameter that quantifies the offset. However, as can be "eyeballed" in Figure 5, the rotators are more closely spaced than those in **4a**,**b**. The situation with the two P−Fe−P axes is similar, for as noted above these are rigorously parallel for **3** and **4a**,**b** but not **5** and **6**. Accordingly, fixed distances can be assigned with the former group but not the latter.

As illustrated in Figure 5, the iron−iron distances in **3** are 5.894(9)−5.782(1) Å (independent molecules 1 and 2), whereas those in **4a**,**b** (6.466(1)−6.403(1) Å), **5** (7.601(3) Å), and **6** (8.517 Å) are progressively longer, reflecting the increasing (CH$_2$)$_n$ tether lengths. However, it should be emphasized that due to the offset of the Fe(C)$_3$ planes, the distances between the P−Fe−P axes are shorter. For complexes **3** and **4a**,**b** where this can be quantified, the trend is *not* monotonic. Rather, **3** (n = 3) and **4b** (n = 4) give essentially identical values (~5.8 Å). All of these factors bear on the potential for Fe(CO)$_3$/Fe(CO)$_3$ interactions, which are further analyzed in the Discussion.

The IR spectrum of crystalline monoiron complex **6′** was identical with that isolated from Scheme 3. The P−Fe−P bond angle, 147.4(2)° (Table 3 and Figure 3), represents a dramatic reduction from the 180° expected for an idealized trigonal bipyramid with *trans*-diaxial phosphine ligands, and the values found for **3** and **4a**,**b** (172.8(1)−178.4(1)°). Thus, **6′** is best regarded as *trans* square pyramidal, with the carbonyl ligand that extends to the left in Figure 3 representing the apical position. These relationships are sketched in Scheme 3. Accordingly, the OC−Fe−CO bond angles are no longer ca. 120° as in the other complexes, but rather 151.8(1)° (for the two basal CO ligands) or 104.7(1)−103.5(1)° (for the apical CO ligand). The same conclusions are reached using other geometric features.[11]

In **6′**, the iron−carbon distances for the two CH$_2$ carbon atoms closest to the plane of the Fe(CO)$_3$ rotator (see Figure 3) are 3.939 and 4.518 Å. When the van der Waals radius of an sp^3 carbon atom[21] is subtracted, "clearances" of 2.24−2.82 Å are obtained. Since these values are well within the radius of the Fe(CO)$_3$ rotator (4.45 Å), a 360° rotation should be impossible (although oscillations of a few degrees may take place).

DFT Computations. Given the established relationship between IR $\nu_{C\equiv O}$ band patterns and structure,[18] and the various ways in which experimental data might be misleading (impurities, mixtures of isomers, crystal vs solution structures, etc.), DFT was utilized to calculate the absorptions for all of the preceding diiron and monoiron complexes. Techniques and functionals that have proved reliable in past studies were employed,[13,22] as detailed further in the Experimental Section and the Supporting Information. In all cases, initial energy minimizations afforded structures very close to those obtained crystallographically, as illustrated in Figures S5 and S6. The IR results are summarized in Table 1 and Figure 6. The IR spectrum of **3′** has been similarly computed in an earlier study.[13]

As shown in Figure 6 (bottom), the title complexes **3**, **4a**,**b**, **5**,[9] and **6** (only characterized computationally given the

Table 3. Key Interatomic Distances (Å) and Bond Angles (deg) for Crystallographically Characterized Complexes

	3·(CH$_2$Cl$_2$)$_4$[a,b]	**4a**·(toluene)$_6$[a,b]	**4b**[a,c]	**6′**·(toluene)$_{0.5}$
Fe1−P1	2.211(1)/2.200(1)	2.213(2)/2.214(2)	2.209(2)	2.214(1)
Fe1−P2	2.211(2)/2.212(1)	2.209(2)/2.207(2)	2.208(2)	2.217(1)
Fe1−C1	1.772(5)/1.778(6)	1.781(8)/1.760(8)	1.784(9)	1.769(2)
Fe1−C2	1.773(4)/1.763(6)	1.752(8)/1.781(7)	1.765(9)	1.775(2)
Fe1−C3	1.776(4)/1.774(4)	1.767(7)/1.765(6)	1.784(9)	1.769(2)
C1−O1	1.160(6)/1.148(7)	1.156(8)/1.170(9)	1.195(1)	1.155(2)
C2−O2	1.160(5)/1.164(7)	1.166(8)/1.163(8)	1.162(1)	1.156(2)
C3−O3	1.157(5)/1.157(5)	1.163(7)/1.162(7)	1.144(1)	1.152(2)
Fe1−O1	2.931(4)/2.926(4)	2.938(6)/2.930(5)	2.928(6)	2.933(1)
Fe1−O2	2.933(3)/2.926(5)	2.919(6)/2.944(5)	2.926(7)	2.931(1)
Fe1−O3	2.933(3)/2.931(3)	2.931(4)/2.927(4)	2.933(6)	2.921(1)
C1−Fe1−C2	115.7(2)/118.7(2)	122.3(3)/122.0(3)	122.2(4)	151.8(1)
C1−Fe1−C3	125.0(2)/122.1(2)	118.3(3)/117.7(3)	120.1(4)	103.5(1)
C2−Fe1−C3	119.3(2)/119.2(2)	119.4(3)/120.3(3)	117.7(4)	104.7(1)
P1−Fe1−P2	174.6(1)/178.4(1)	172.8(1)/174.3(1)	176.8(1)	147.4(2)

[a]The diiron complexes feature inversion centers that exchange primed and unprimed atoms (see Figure 2). [b]Values are given for each of the two independent molecules (1,2) in the unit cell. [c]See Experimental Section for information on solvent in the lattice.

Table 4. Additional Structural Features of Crystallographically or Computationally Characterized Diiron Complexes^{a}

complex (method)	**3**·(CH$_2$Cl$_2$)$_4$ (XRD)^{b,c}	**4a**·(toluene)$_6$ (XRD)^{b,c}	**4b** (XRD)^{b,d}	**5**·(CH$_2$Cl$_2$)$_2$ (XRD)^{e}	**6** (DFT)
radius Fe(CO)$_3$ rotator^{f}	4.45/4.45	4.45/4.45	4.45	4.45	4.47
Fe1···Fe1′^{g}	5.894(9)/5.782(1)	6.403(1)/6.466(1)	6.151(2)	7.601(3)	8.517
P1···P2^{g}	4.417(2)/4.412(2)	4.414(2)/4.416(2)	4.415(3)	4.422(3)	4.455
P1···P2′^{g}	5.703(1)/5.722(2)	6.597(2)/6.599(2)	6.128(3)	7.539(4)	8.452
O1···O3′^{g}	3.308(5)/3.007(5)	3.677(8)/3.610(7)	3.432(1)	6.723(1)^{h}	5.531
O3···O3′^{g}	5.284(5)/5.954(5)	4.546(7)/5.285(7)	6.531(9)	6.913(1)^{h}	7.738
P1−Fe1−P2/Fe1′ vs P1′−Fe1′−P2′/Fe1^{i}	0.00/0.00	0.00/0.00	0.00	7.67	12.00
P2−Fe1−Fe1′−P1′^{j}	2.1/−0.2	5.3/4.7	−3.3	−7.7	−10.8
P2−Fe1−Fe1′−P2′^{j}	180.0/−180.0	−180.0/180.0	180.0	171.0	167.8
P1−Fe1−Fe1′−P2′^{j}	−2.1/0.2	−5.3/−4.7	3.3	−7.7	−13.3
P1′−Fe1′−Fe1−P1^{j}	−180.0/180.0	−180.0/180.0	−180.0	173.7	168.2
Fe1−P2−C4−C5^{j}	57.4/−42.3	−70.3/−70.0	80.1	60.3	63.4/68.6
P2−C4−C5−C6^{j}	−177.6/166.3	111.9/104.8	−136.2	173.9	159.2/−169.7
C4−C5−C6−C7^{j}		178.3/−179.7	74.1	66.3	65.2/67.5
C5−C6−C7−C8^{j}				164.5	76.0/170.5
C6−C7−C8−C9^{j}					63.2/−63.0
$C_{\omega-2}$−$C_{\omega-1}$−C_{ω}−P1′^{j,k}	162.8/−175.3	−174.6/−167.1	163.1	−174.9	155.31/−137.2
$C_{\omega-1}$−C_{ω}−P1′−Fe1′^{j,l}	−46.2/50.9	−70.5/−71.6	−175.1	54.5	64.42/74.05
P1−Fe1−P2/P1′−Fe1′−P2′ axis/axis distance^{m}	5.884/5.780	6.166/6.400	5.853	n	n
offset of rotators Fe1(C)$_3$/Fe1′(C′)$_3$^{m}	0.087/0.029	0.980/1.209	1.665	n	n

[a] Quantities not available from the crystallographic output were calculated using standard programs such as Mercury. [b] These complexes feature inversion centers that exchange primed and unprimed atoms (see Figure 2). [c] Values are given for each of the two independent molecules (1, 2) in the unit cell. [d] See the Experimental Section for information on solvent in the lattice. [e] From ref 9. [f] Calculated by averaging the Fe−O distances and adding the van der Waals radius of oxygen (1.52 Å). [g] Nonbonded distance (Å). [h] These values are for O1···O1′ and O3···O1, respectively (the crystallographic C_2 symmetry of this compound necessitates minor changes in atom numbering). [i] Angle between two four-atom least-squares planes (deg). [j] Torsion angle (deg). [k] This torsion angle is the counterpart to P2−C4−C5−C6; ω = 6, 7, 7, 8, and 9 for the respective entries. [l] This torsion angle is the counterpart to Fe1−P2−C4−C5; ω = 6, 7, 7, 8, and 9 for the respective entries. [m] Due to the inversion centers in **3**·(CH$_2$Cl$_2$)$_4$, **4a**·(toluene)$_6$, and **4b**, the two axes or planes are parallel with a constant intervening distance (Å). [n] Due to the absence of inversion centers in **5** and **6**, the P−Fe−P axes and Fe(C)$_3$ planes are not parallel, and unique separations cannot be assigned. Figure 5 allows visual estimates.

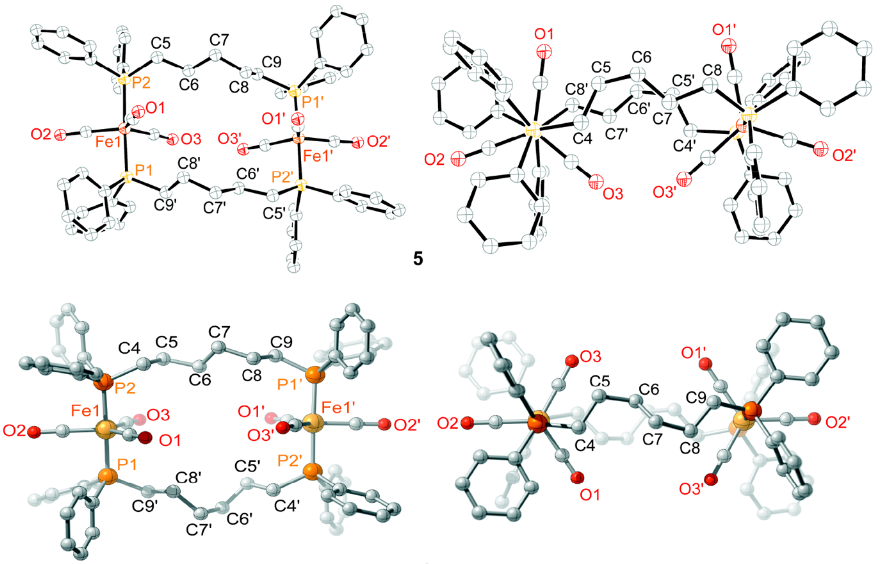

5

6

Figure 4. Thermal ellipsoid plots (50% probability) of the previously reported molecular structure of **5** (top)[9] and a plot of the computed structure for the yet unknown higher homologue **6** (bottom). The primed atoms in the latter (employed for uniformity with the other structures) are misleading as there are no symmetry elements.

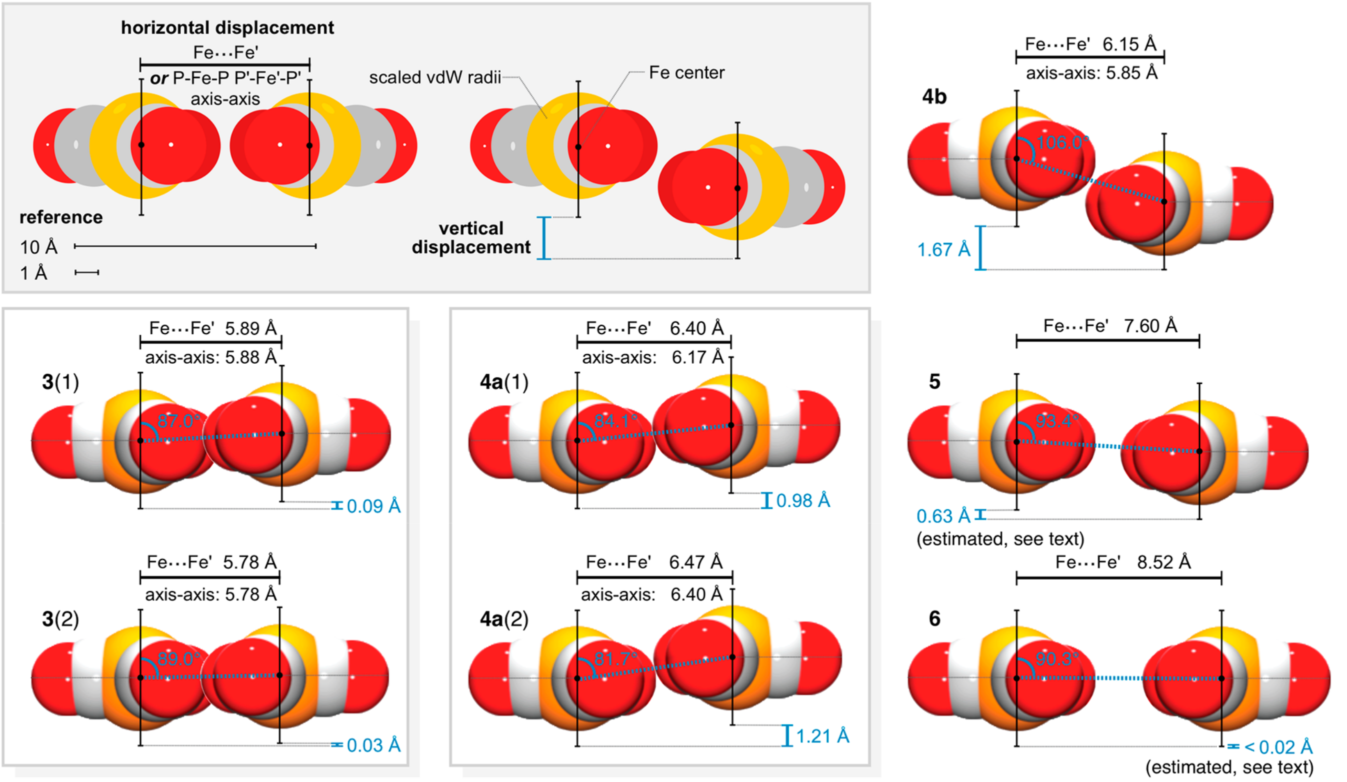

Figure 5. Space-filling side views of the $Fe(CO)_3$ rotators in **3** (two independent molecules (1 and 2)), **4a** (two independent molecules (1 and 2)), and **4b**, **5**, and **6** (computed structure) illustrating the offset between the two $Fe(CO)_3$ planes and iron–iron and (when constant) P–Fe–P axis–axis distances.

isolation of **6′**) are predicted to exhibit three vibrational modes (a–c), each with the $Fe(CO)_3$ units strongly coupled. The lowest frequency band (corresponding to c) is always the most intense, and shifts randomly within a 26 cm^{-1} range as n increases from 3 to 6 (1876, 1867/1862, 1865, 1893 cm^{-1}). These bands are furthermore predicted to exhibit shoulders at slightly higher frequencies (4–13 cm^{-1}, corresponding to b). However, in computations the peaks can be narrowed or broadened per the line width selected, as illustrated in Figure 6 (compare the inset with 8 cm^{-1} line widths to the other spectra with 4 cm^{-1} line widths). Thus, these shoulders may or may not be visible experimentally (they are seen for **3** and **4b**). There is no dipole moment change associated with the third highest frequency vibrational mode (a). Hence, these are formally IR-inactive. Nonetheless, weak absorptions are observed experimentally for **3** and **4a**,**b** (1964–1969 cm^{-1}).

Next, we focus on the spectra of monoiron complexes **3′**, **4′a**, **5′**, and **6′** depicted in Figure 6 (top). These feature different coordination geometries as summarized in Table 1 and represented in Figure 6 as **VI′** (tbp *cis*), **VI″** (sq pyr *cis*), and **VI‴** (sq pyr *trans*). Complex **6′**, new to this study and possessing the rare geometry **VI‴**, is predicted to exhibit three IR $\nu_{C\equiv O}$ bands. However, the two lowest frequency bands (1865 s, 1892 m cm^{-1}) apparently merge into a single band experimentally (1863 cm^{-1}). In any case, the weak highest frequency band is reproduced (1941 vs 1965 cm^{-1}),

The IR $\nu_{C\equiv O}$ bands computed for the remaining monoiron complexes are in excellent agreement with those found experimentally. Furthermore, coordination modes **VI′** and **VI″** give quite similar patterns, with three bands of strong to medium intensities. However, the most important conclusion is that an impurity of this type should be apparent in the IR spectrum of a diiron complex. For example, the highest frequency bands are intense in the monoiron complexes (1984–1981 cm^{-1}) but very weak in the diiron complexes (1969–1965 cm^{-1}).

In the course of computing the IR spectra, total energies corresponding to the most stable form of each iron complex were obtained (both gas and solution phase). These allow the free energies for the monoiron/diiron complex equilibria shown in Scheme 4 to be calculated. Interestingly, the diiron complexes are always the more stable, at least for the range of n examined.

■ DISCUSSION

Syntheses. The preceding results, together with literature data, indicate that the $Fe(CO)_3$ source and conditions associated with Scheme 2 have a profound influence upon the type of product obtained. In our first cycle of experiments with the diphosphines $Ar_2P(CH_2)_nPAr_2$, only the target diiron tetraphosphorus complexes (**V**) were detected. However, as these reactions were investigated by additional co-workers, with the usual minor variances in conditions, it became apparent that monoiron diphosphorus complexes **VI** could also form. From a different direction, several other groups have reported reactions of $Fe(CO)_3$ sources and the diphosphine $Ph_2P(CH_2)_3PPh_2$.[13,14b–d] In contrast to our results, only the monoiron complex **3′** was isolated.

So far, only Liu and Goh, in their studies with $Ph_2P(CH_2)_5PPh_2$, have been able to optimize conditions for either type of product.[9] In refluxing THF, the maleic acid (MA) adduct $(MA)Fe(CO)_4$ and the amine oxide $Me_3N^+{-}O^-$ afford

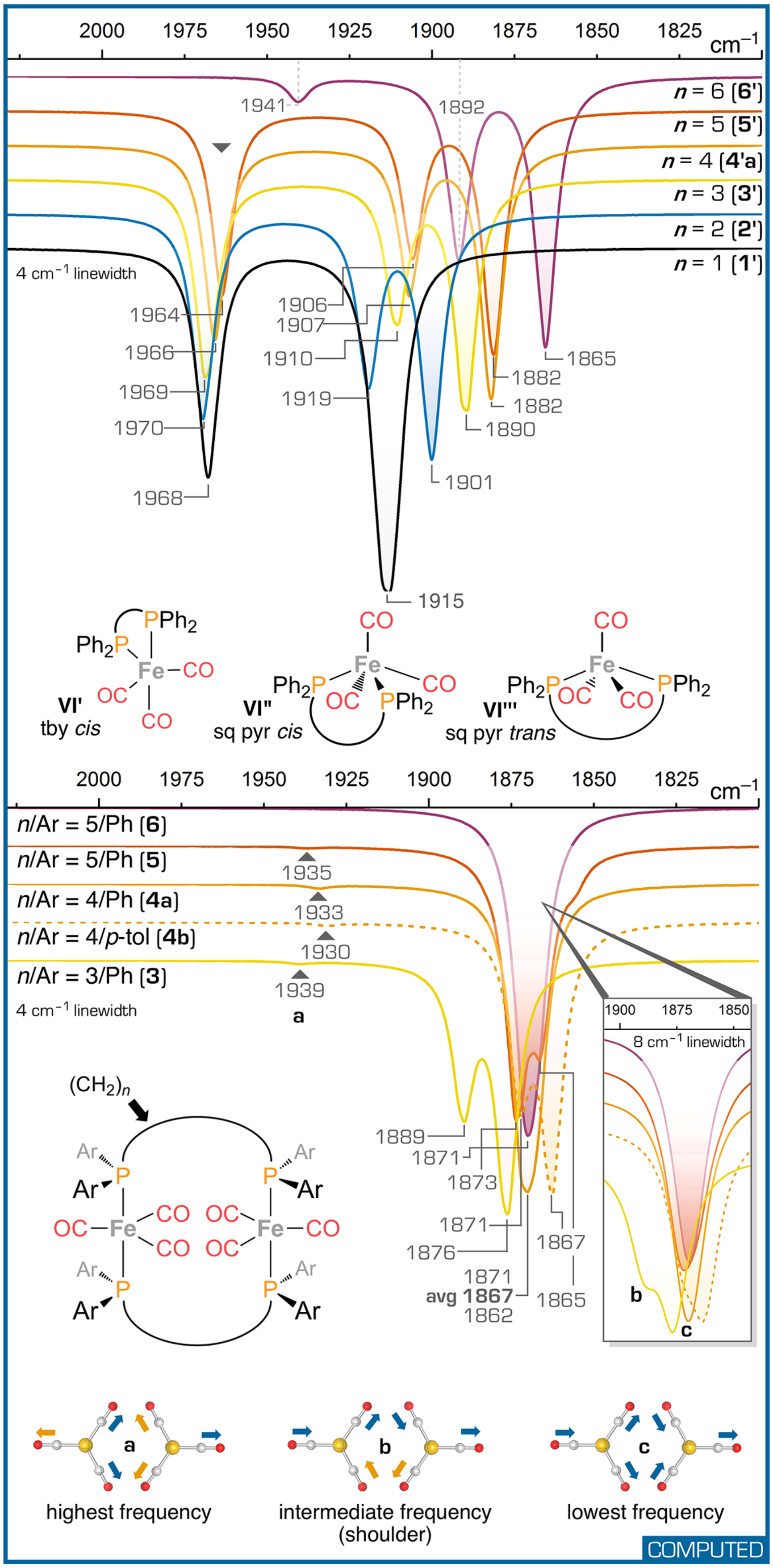

Figure 6. Computed IR $\nu_{C\equiv O}$ bands for monoiron and diiron carbonyl complexes.

Scheme 4. Computed Δ*G* Values for the Hypothetical Equilibrium between Monoiron and Diiron Complexes

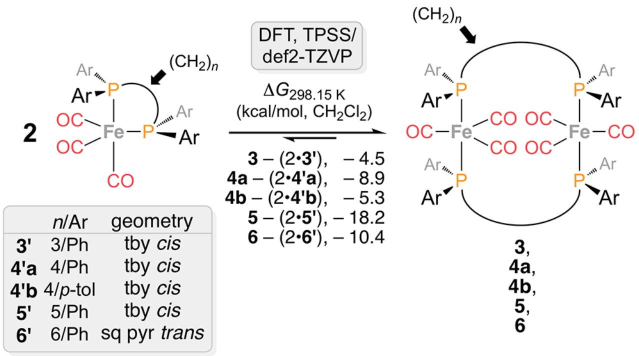

	n/Ar	geometry
3'	3/Ph	tby *cis*
4'a	4/Ph	tby *cis*
4'b	4/*p*-tol	tby *cis*
5'	5/Ph	tby *cis*
6'	6/Ph	sq pyr *trans*

the diiron complex **5** in 45% yield, as depicted in Scheme 3 (bottom). In contrast, the cyclooctene (COE) adduct $(COE)_2Fe(CO)_3$ gives the monoiron product **5′** in 93% yield (−60 °C to RT, THF). There is presently no rationale for this dichotomy. The higher temperature reaction affords the more stable product, **5**, according to the computational data in Scheme 4. However, **5′** is recovered unchanged after 2 days when subjected to these conditions.[9]

Steric Interactions in Diiron Complexes. With regard to the main objectives of this study, the most important structural features are those that affect correlated $Fe(CO)_3/Fe(CO)_3$ rotation or gearing. Thus, it is encouraging to see parallel or nearly parallel P−Fe−P axes maintained throughout the series **3**, **4a**,**b**, **5**, and **6** in Figures 2 and 4. However, as the lengths of the $(CH_2)_n$ tethers increase, potential structural motifs multiply.

For example, conformations with nonparallel axes or twisted endgroups are likely to become increasingly accessible. Alternatively, the planes of the $Fe(CO)_3$ rotators can become increasingly offset, such that they no longer efficiently engage. In this study, the maximum separation is found with **4b** (1.67 Å; Table 4 and Figure 5), which is comparable to the van der Waals radii of carbon and oxygen atoms (1.70 Å, 1.52 Å). When the offset reaches the van der Waals *diameters* of the CO ligands, the two rotators can no longer sterically engage.

The offsets have their origins in the conformations of the $FeP(CH_2)_nPFe$ segments. In both independent molecules of **3**, the two FePCC units have *gauche* conformations (torsion angles ±42−57°; see Table 4), and the two PCCC units have *anti* conformations (torsion angles ±178−166°), as easily visualized in Figure 2. Alternative *gauche*/*anti* patterns are highly unlikely. However, the longer $FeP(CH_2)_4PFe$ segments in **4a**,**b** allow two different motifs. In both molecules of **4a**, the two FePCC units remain *gauche* (torsion angles −70° to −72°). The CCCC units and one PCCC unit are *anti* (±167−180°), whereas the other PCCC unit adopts an intermediate conformation (105−112°). In contrast, with **4b**, one FePCC unit becomes *anti* (−175°), while the other remains *gauche* (80°). The former catapults a methylene group much further from the rotator plane (Figure 2, bottom), rendering a greater offset more likely. The adjacent PCCC unit is approximately *anti* (−136°), and to close the ring the CCCC unit must adopt a *gauche* conformation (74°).

In summary, the *anti* FePCC unit in **4b** can be viewed as introducing a "stair step" that increases the likelihood of significantly offset $Fe(CO)_3$ rotators. In solution, one could logically expect **4a** and **4b** to sample both types of conformations as well as others. The $FeP(CH_2)_nPFe$ conformations of **5** and **6** are not analyzed in similar detail, but a casual inspection of Figure 4 shows increasingly complex torsion angle patterns that at some value of *n* would promote P−Fe−P axes that are distinctly nonparallel.

With regard to steric interactions between the $Fe(CO)_3$ rotators in **3**, **4a**,**b**, **5**, and **6**, the starting point for analysis is the van der Waals radii of the rotators (4.45 Å; Table 4). In order to ensure that two parallel and coplanar rotators never sterically interact, the P−Fe−P axes must be spaced by twice this amount, or 8.90 Å. Of all of the diiron complexes considered in this study, only **6**, with an iron−iron distance of 8.517 Å, approaches this limit.

Top views of the $Fe(CO)_3$ rotators in **3** and **4a**,**b** are given in Figure 7. Interestingly, only in one case are there van der Waals contacts. In viewing such projections, it should be kept in mind that per Figure 5, none of the neighboring $Fe(CO)_3$ units are strictly coplanar with respect to each other. Thus, as noted above, the distances between the parallel P−Fe−P axes are shorter than the iron−iron distances.

Next, we consider the arbitrary $Fe(CO)_3/Fe(CO)_3$ orientation in panel A of Figure 8, which has no crystallographic counterpart in Figure 7. This can be viewed as a head-to-tail arrangement of two rotators with respect to two Fe−CO vectors. In these analyses, the $Fe(CO)_3$ units are constrained to be *coplanar*, so the iron−iron and P−Fe−P axis separations are identical. These distances are reduced until there is van der Waals contact between the two rotators, which occurs at an iron−iron separation of 6.67 Å. Interestingly, the approach is limited not by the van der Waals radii of the iron atom or carbonyl oxygen, but rather the carbonyl carbon (see inset).

In panel B of Figure 8, the iron−iron distance in panel A is maintained, but the $Fe(CO)_3$ rotator on the left is rotated by

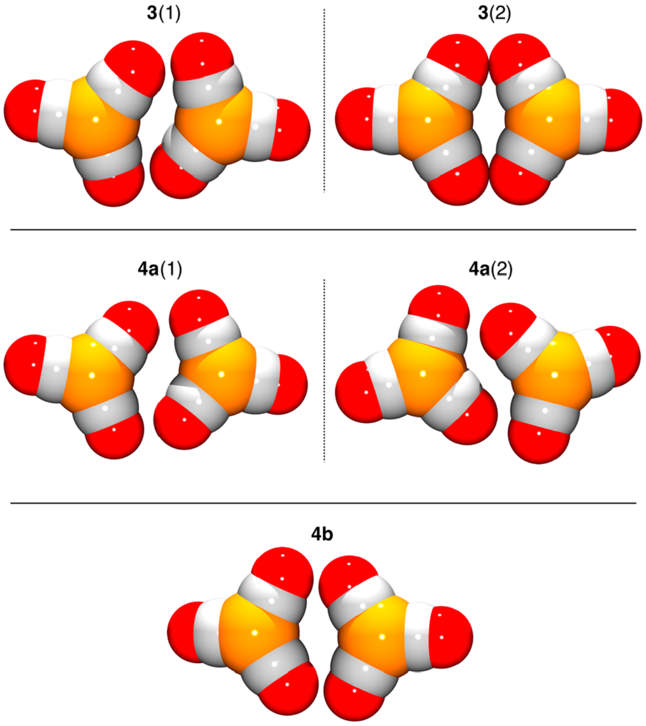

Figure 7. Space-filling "top" views of the $Fe(CO)_3$ rotators of **3** (top, both independent molecules), **4a** (middle, both independent molecules), and **4b** (bottom) at van der Waals radii.

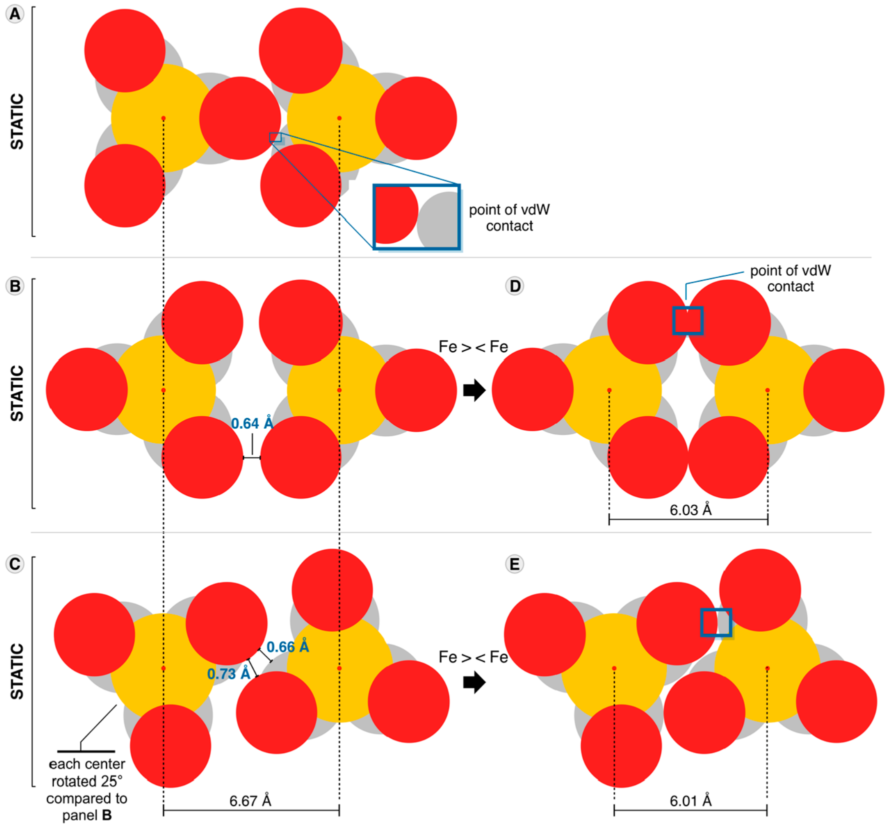

Figure 8. Analyses of interactions in hypothetical conformations of complexes with two coplanar $Fe(CO)_3$ rotators (see text).

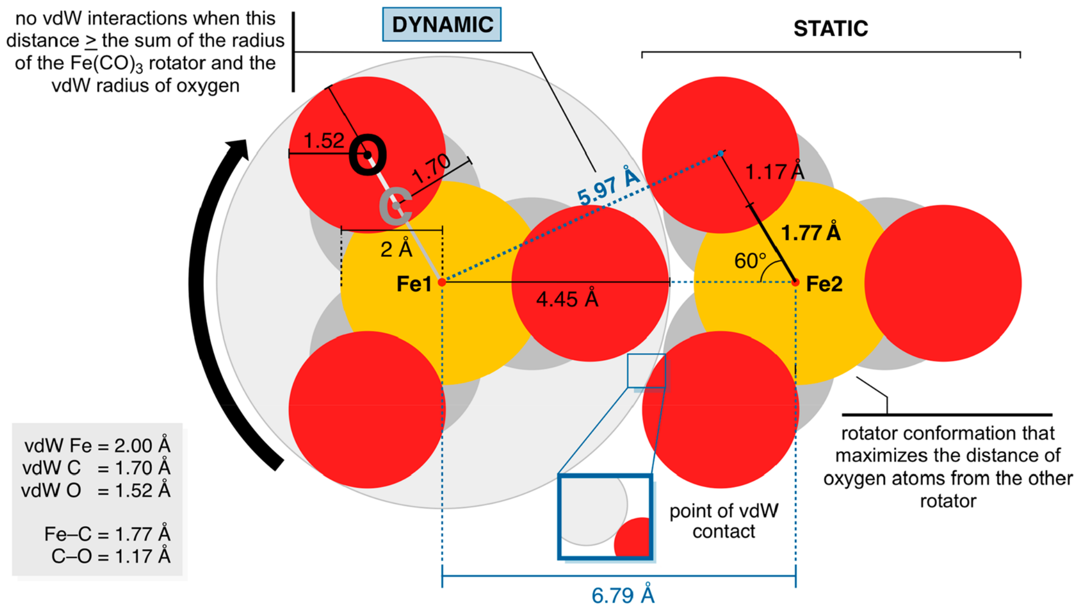

Figure 9. Minimum iron/iron spacing required (6.79 Å) for rotation of a $Fe(CO)_3$ rotator with no van der Waals (vdW) interactions with a neighboring $Fe(CO)_3$ rotator.

180° to give a tail-to-tail orientation of the two Fe−CO vectors, as seen in the crystal structures of **3**(2) and **4b**. This opens up some void space between the rotators, which at the narrowest is 0.64 Å (CO···OC). As shown in panel C, a variant is then considered in which both rotators have been rotated clockwise by 25°, approximating other orientations in Figure 7 (**3**(1), **4a**(1), and **4a**(2)). Now the void space narrows to 0.73 Å (CO···OC) and 0.65 Å (CO···C).

Next, the $Fe(CO)_3$ conformations in panels B and C were maintained but the iron−iron distances were compressed until the onset of van der Waals contacts. As shown in panels D and E, separations of 6.03−6.01 Å could be realized. We suggest that these represent realistic "minimum contacts" for coplanar $Fe(CO)_3$ rotators. Of course, at such distances gearing would likely be frozen. It is more challenging to define an iron−iron distance at which gearing would be optimal.

Scheme 5. A Triphosphine That Templates the Synthesis of Trinickel Complexes with Three Approximately Parallel Rotators

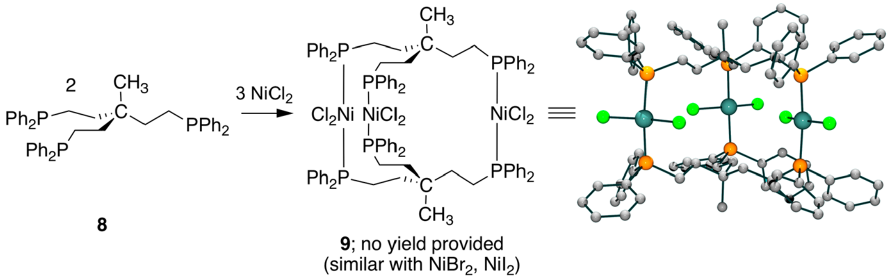

One approach is to define additional limiting values. For example, what is the minimum iron–iron distance at which one $Fe(CO)_3$ rotator can experience sterically barrierless rotation (i.e., no van der Waals contacts) with respect to the other? This is addressed in Figure 9, where the $Fe(CO)_3$ on the right (Fe2) is kept static, with the CO ligands as far removed from the $Fe(CO)_3$ on the left (Fe1) as possible. For example, rotating Fe2 slightly clockwise or counterclockwise from the orientation depicted would force one of the two CO oxygen atoms directed toward Fe1 still closer to Fe1.

Accordingly, Fe1 and the proximal CO oxygen atom from Fe2 must have a steric clearance that matches the sum of the radius of the $Fe(CO)_3$ rotator and the van der Waals radius of the CO oxygen atom, 5.97 Å (4.45 + 1.52 Å). Applying standard trigonometric relationships, this corresponds to a Fe1–Fe2 separation of 6.79 Å. Said differently, this is the closest iron–iron approach for which one $Fe(CO)_3$ can rotate independently of the other (although van der Waals contacts will ensue with any other Fe2 conformation). One take-home message from Figures 8 and 9 is that the "sweet spot" for gearing involves a narrow range of iron–iron distances, perhaps on the order of 6.70–6.50 Å. Other approaches to defining optimal spacings for gears derived from trigonal rotators have been described by Baldridge and Siegal, who have defined concepts such as gearing fidelity.[3a] They also emphasize issues with treating atoms as "hard spheres", possible roles of dispersion forces, and a host of other factors.

Related Complexes and Directions. Several attributes of new square pyramidal monoiron complex **6′** also merit note. First, it features the shortest methylene chain capable of bridging two trans phosphorus donor atoms for any coordination geometry.[23,24] Interestingly, a similar complex, **6″**, with a diphosphine derived from 2,2′-dimethylbiphenyl has been reported by Casey, the crystal structure of which is shown in Figure 3 (right).[25] As with **6′**, six carbon atoms tether the trans phosphorus donor atoms, but most are sp^2 hybridized.

The P–Fe–P and basal CO–Fe–CO bond angles in **6″** (152.0(1) and 141.8(4)°), are close to those of **6′** (147.4(2) and 151.8(1)°). As with **6′**, the IR spectrum shows one strong $\nu_{C\equiv O}$ band (1882 cm^{-1}) and a second weaker band at a higher frequency (1970 cm^{-1}).[25] However, with **6″** only a single CO $^{13}C\{^1H\}$ NMR signal is observed at −80 °C, in contrast to the two found at ambient probe temperature for **6′**.[25] As noted above, the close Fe···(CH_2) contacts in **6′** seemingly block $Fe(CO)_3$ rotation, and the crystallographic data for **6″** deliver an analogous prediction. Other mechanisms for ^{13}C NMR signal coalescence would include rapid and reversible CO dissociation.

With regard to bimetallic complexes with sterically coupled rotors, as embodied by **III** in Scheme 1, the synthetic strategy applied in Scheme 2 is not limited to $Fe(CO)_3$ sources or trigonal bipyramidal adducts. Indeed, α,ω-diphosphines $Ph_2P(CH_2)_nPPh_2$ have also been used to template the synthesis of analogous square planar adducts *trans*,*trans*-L′LM[$Ar_2P(CH_2)_nPAr_2$]$_2$MLL′, for example, with M/n = Rh/1–4.[26]

There is also grounds for cautious optimism with regard to extending this synthetic strategy to arrays with increased numbers of rotators. As shown in Scheme 5, combination of the triphosphine $CH_3C(CH_2CH_2PPh_2)_3$ (**8**) with $NiCl_2$ affords the 2:3 trinickel hexaphosphorus adduct **9**, with three roughly parallel P–Ni–P axes.[27] Here the phosphorus atoms are connected by five-carbon bridges. In principle, the degree of steric communication between the rotators could be fine-tuned by adjusting this spacing or varying the chloride ligands.

However, as detailed in the preceding analyses, the conformational flexibility of these types of diphosphine or triphosphine ligands present challenges with regard to precisely controlling rotator/rotator interactions. As illustrated by **4a** and **4b** in Figures 2 and 5, even when the $(CH_2)_n$ tethers are of equal lengths, the iron–iron distances, P–Fe–P axis separations, and distances between the planes of the two rotators can vary considerably. A second-generation approach would involve more rigid diphosphines with fewer degrees of freedom, as might be realized with a cyclohexane containing ligand with two 1,3-diaxial PAr_2 moieties. Such building blocks would seemingly enforce coplanar $Fe(CO)_3$ rotors and parallel P–Fe–P axes.

■ CONCLUSION

This study has shown that it is possible to access diiron tetraphosphorus systems of the type **V** directly from $Fe(CO)_3$ sources and diphosphines $Ar_2P(CH_2)_nPAr_2$ with n = 3 and 4 (Schemes 2 and 3). These results augment an earlier report of an adduct with n/Ar = 5/Ph.[9] The short $Fe(CO)_3$/$Fe(CO)_3$ distances in these systems lead to steric interactions. The current NMR data suggest very high rotational barriers in **3** and lower barriers likely involving correlated rotation in **4a**,**b**. However, preliminary experiments show that a rigorous interrogation of these processes is best approached with ^{13}CO labeled substrates or perhaps via lower symmetry isosteric systems that feature one or more CO/NO^+ substitutions.[7] Thus, no additional data regarding dynamic properties are presented at this time. Additionally, as noted in the preceding section, other types of diphosphines with fewer degrees of conformational freedom may afford adducts with more efficient rotator/rotator coupling.

The computational data further show that the diiron tetraphosphorus complexes **V** are thermodynamically more stable than all of the possible coordination geometries of the monoiron diphosphorus complexes **VI**. They also establish diagnostic IR $\nu_{C\equiv O}$ band patterns for the diiron complexes that allow structures to be verified for crystalline and noncrystalline samples as well as in solution where dynamic NMR properties may be probed. Although other potential applications for the new diiron and monoiron carbonyl compounds should not be overlooked,[28] this work has provided a detailed foundation for further studies of interactive Fe(CO)$_3$/Fe(CO)$_3$ rotators. Finally, extensions of these themes to triiron, tetrairon, and higher systems are easily envisioned, where there are intriguing possibilities for "water wheels" and other types of molecular machines.

■ EXPERIMENTAL SECTION

General. All reactions and workups were conducted under inert atmospheres using oven-dried glassware. Solvents were purified using a Glass Contour system; CDCl$_3$ and DMSO-d_6 (2 × Cambridge Isotopes) were freeze−pump−thaw degassed. The diphosphines Ph$_2$P(CH$_2$)$_n$PPh$_2$ (n = 3, TCI; n = 4 and 6, Alfa-Aesar), P(p-tol)$_3$ (Strem), n-BuLi (2.5 M in hexane, Sigma-Aldrich), 1,4-dibromobutane (Alfa-Aesar), and silica (Silicycle, 40−63 μm, 230−400 mesh), were used as received. (BDA)Fe(CO)$_3$ was prepared by a literature procedure.[15]

NMR spectra were recorded on standard FT instruments at ambient probe temperatures and referenced as follows (δ, ppm): ^{1}H, residual internal CHCl$_3$ (7.27) or DMSO-d_5 (2.50); ^{13}C {^{1}H}, internal CDCl$_3$ (77.00) or DMSO-d_6 (39.52); ^{31}P{^{1}H}, external 85% H$_3$PO$_4$ (0.00). IR spectra were recorded using a Shimadzu IRAffinity-1 spectrometer with a Pike MIRacle ATR system (diamond/ZnSe crystal). Microanalyses were conducted by Atlantic Microlab. Electrospray ionization mass spectrometry (ESI-MS) was carried out with a Thermo Scientific Q Exactive Focus instrument.

(p-tol)$_2$P(CH$_2$)$_4$P(p-tol)$_2$. A Schlenk flask was charged with a solution of P(p-tol)$_3$ (2.0 g, 6.7 mmol) in THF (17 mL) and cooled to 0 °C. Then n-BuLi (2.7 mL, 6.67 mmol, 2.5 M in hexane) was added dropwise with stirring. After 1 h, the cold bath was removed, and the bright red mixture transferred by cannula to a solution of 1,4-dibromobutane (0.723 g, 3.35 mmol) in THF (13 mL). After 16 h, the solvent was removed by oil-pump vacuum. Hexane was added, and the sample filtered through a pad of silica (3 × 5 cm) that was rinsed with 2:1 v/v hexane/CH$_2$Cl$_2$ and then CH$_2$Cl$_2$. The solvent was removed from the CH$_2$Cl$_2$ rinses by oil-pump vacuum to give (p-tol)$_2$P(CH$_2$)$_4$P(p-tol)$_2$ as a white solid (0.759 g, 1.57 mmol, 47%). Mp 120.8−122.9 °C. Anal. Calcd (%) for C$_{32}$H$_{36}$P$_2$ (482.58): C, 79.64; H, 7.52. Found: C, 79.92; H, 7.53.

NMR (CDCl$_3$, δ in ppm):[29] ^{1}H (500 MHz) 7.33−7.27 (m, 8H, o to P), 7.17−7.13 (m, 8H, m to P), 2.36 (s, 12H, CH$_3$), 2.00 (br t, $^3J_{\mathrm{HH}}$ = 6.9 Hz, 4H, PCH$_2$) 1.59−1.51 (m, 4H, CCH$_2$C); ^{13}C{^{1}H} (125 MHz) 138.3 (s, p to P), 135.4 (d, $^1J_{\mathrm{CP}}$ = 12.3 Hz. i to P), 132.6 (d, $^2J_{\mathrm{CP}}$ = 18.8 Hz, o to P), 129.1 (d, $^3J_{\mathrm{CP}}$ = 7.1 Hz, m to P), 28.0 (d, $^1J_{\mathrm{CP}}$ = 10.7 Hz, PCH$_2$), 27.7 (t, $^2J_{\mathrm{CP}}$ = 14.8 Hz, PCH$_2\underline{\mathrm{C}}$H$_2$), 21.3 (s, CH$_3$); ^{31}P{^{1}H} (162 MHz) −18.2 (s). IR (powder film, cm^{-1}): 2963 (w), 1558 (w), 1258 (m), 1089 (m), 1013 (s), 793 (s).

***trans,trans*-(CO)$_3$Fe[Ph$_2$P(CH$_2$)$_3$PPh$_2$]$_2$Fe(CO)$_3$ (3).** A Schlenk flask was charged with (BDA)Fe(CO)$_3$ (0.200 g, 0.699 mmol), Ph$_2$P(CH$_2$)$_3$PPh$_2$ (0.236 g, 0.573 mmol), and THF (7.4 mL) with stirring and covered with aluminum foil. A yellow precipitate formed. After 48 h, the solvent was removed by oil-pump vacuum, and cold THF was added. The mixture was filtered through a pad of silica (3 × 5 cm) that was rinsed first with cold THF and then with toluene. The solvent was removed from the yellow toluene rinses by oil-pump vacuum to give **3** as a pale yellow solid (0.139 g, 0.126 mmol, 44% of theory (0.573/2 mmol)) that decomposed to a black solid at >153 °C. Anal. Calcd (%) for C$_{60}$H$_{52}$Fe$_2$O$_6$P$_4$ (1048.21): C, 65.24; H, 4.75. Found: C, 65.86; H, 4.73.

NMR (DMSO-d_6, δ in ppm): ^{1}H (500 MHz) 7.71−7.65 (br m, 16H, C$_6$H$_5$), 7.52−7.44 (m, 24H, C$_6$H$_5$), 2.75−2.65 (br m, 8H, PCH$_2$), 2.39−2.28 (br m, 4H, PCH$_2$C$\underline{\boldsymbol{H}}_2$). ^{13}C{^{1}H} (125 MHz, cryoprobe)[30] 214.7 (apparent m, CO), 212.4 (apparent m, CO), 136.7 (apparent m, i to P), 131.2 (br s, w$_{1/2}$ 37 Hz, o to P), 129.9 (s, p to P), 128.4 (br s, w$_{1/2}$ 34 Hz, m to P), 33.8 (apparent m, PCH$_2$), 21.5 (s, PCH$_2\underline{\mathrm{C}}$H$_2$). ^{31}P{^{1}H} (202 MHz) 75.12 (s). IR (powder film, cm^{-1}): 3068 (w), 2959 (w), 1969 (w, $\nu_{\mathrm{C}\equiv\mathrm{O}}$), 1892 (sh, $\nu_{\mathrm{C}\equiv\mathrm{O}}$), 1871 (s, $\nu_{\mathrm{C}\equiv\mathrm{O}}$), 1433 (m), 1092 (m), 957 (m), 795 (m), 745 (m), 692 (s), 633 (s). HRMS (ESI, m/z): calcd for C$_{60}$H$_{52}$Fe$_2$O$_6$P$_4$ [M + H]$^+$: 1105.1441. Found: 1105.1449.

***trans,trans*-(CO)$_3$Fe[Ph$_2$P(CH$_2$)$_4$PPh$_2$]$_2$Fe(CO)$_3$ (4a).** (BDA)Fe(CO)$_3$ (0.500 g, 1.75 mmol), Ph$_2$P(CH$_2$)$_4$PPh$_2$ (0.611 g, 1.43 mmol), and THF (19 mL) were combined in a procedure analogous to that for **3**. An identical workup gave **4a** as a yellow solid (0.153 g, 0.135 mmol, 19% of theory (1.43/2 mmol)) that decomposed to a black solid at ≥118 °C. Anal. Calcd (%) for C$_{62}$H$_{56}$Fe$_2$O$_6$P$_4$ (1076.24): C, 65.74; H, 4.98. Found: C, 65.14; H, 5.20.[31]

NMR (CDCl$_3$, δ in ppm): ^{1}H (500 MHz) 7.69−7.52 (br m, 16H, C$_6$H$_5$), 7.46−7.30 (br m, 24H, C$_6$H$_5$), 2.67 (br apparent s, 8H, PCH$_2$), 1.81 (br apparent s, 8H, PCH$_2$C$\underline{\boldsymbol{H}}_2$). ^{13}C{^{1}H} (125 MHz)[30,32] 214.0 (very weak s, tentative CO), 137.5−137.1 (apparent m, i to P), 131.9 (virtual t, $^2J_{\mathrm{CP}}$ = 4.8 Hz, o to P), 129.4 (s, p to P), 128.0 (virtual t, $^3J_{\mathrm{CP}}$ = 4.6 Hz, m to P), 29.5 (apparent m, PCH$_2$), 25.6 (apparent m, PCH$_2\underline{\mathrm{C}}$H$_2$). ^{31}P{^{1}H} (202 MHz) 73.96 (s). IR (powder film, cm^{-1}): 3054 (w), 2965 (w), 1964 (w, $\nu_{\mathrm{C}\equiv\mathrm{O}}$), 1864 (s, $\nu_{\mathrm{C}\equiv\mathrm{O}}$), 1434 (m), 1093 (m), 1014 (m), 794 (m), 743 (m), 694 (s), 633 (s). HRMS (ESI, m/z): calcd for C$_{62}$H$_{56}$Fe$_2$O$_6$P$_4$ [M + H]$^+$, 1133.1754. Found, 1133.1775.

***trans,trans*-(CO)$_3$Fe[p-tol)$_2$P(CH$_2$)$_4$P(p-tol)$_2$]$_2$Fe(CO)$_3$ (4b).** A Schlenk flask was charged with (BDA)Fe(CO)$_3$ (0.500 g, 1.75 mmol), (p-tol)$_2$P(CH$_2$)$_4$P(p-tol)$_2$ (0.690 g, 1.43 mmol), and THF (19 mL) with stirring and covered with aluminum foil. After 48 h, the solvent was removed from the red solution by oil-pump vacuum. Then, 2:1 v/v hexane/CH$_2$Cl$_2$ was added, and the mixture was filtered through a pad of silica (3 × 5 cm). The solvent was removed from the filtrate by oil-pump vacuum to give **4b** as a pale yellow solid (0.498 g, 0.400 mmol, 56% of theory (1.43/2 mmol)) that decomposed to a black solid at >146 °C. Although the ^{13}C {^{1}H} NMR spectrum suggested a high purity (≥96%), the ^{1}H NMR spectrum indicated a somewhat lower value (ca. 90%).[33]

NMR (CDCl$_3$, δ in ppm): ^{1}H (500 MHz) 7.56−7.39 (br m, 16H, C$_6$H$_4$), 7.19 (br apparent s, 16H, C$_6$H$_4$), 2.47 (br apparent s, 24H, CH$_3$), 2.38 (br apparent s, 8H, PCH$_2$), 1.73 (br apparent s, 8H, PCH$_2$C$\underline{\boldsymbol{H}}_2$). ^{13}C{^{1}H} (125 MHz)[32] 220.7 (t, $^2J_{\mathrm{CP}}$ = 8.7 Hz, CO), 139.3 (s, p to P), 135.8 (virtual t, $^1J_{\mathrm{CP}}$ = 21.9 Hz, i to P), 131.9 (virtual t, $^2J_{\mathrm{CP}}$ = 5.2 Hz, o to P), 128.9 (virtual t, $^3J_{\mathrm{CP}}$ = 4.7 Hz, m to P), 32.3 (virtual t, $^1J_{\mathrm{CP}}$ = 11.9 Hz, PCH$_2$), 23.6 (s, PCH$_2\underline{\mathrm{C}}$H$_2$), 21.2 (s, CH$_3$). ^{31}P{^{1}H} (202 MHz) 71.34. IR (powder film, cm^{-1}): 3019 (w), 2923 (w), 2858 (w), 1965 (w, $\nu_{\mathrm{C}\equiv\mathrm{O}}$), 1889 (sh, $\nu_{\mathrm{C}\equiv\mathrm{O}}$), 1870 (s, $\nu_{\mathrm{C}\equiv\mathrm{O}}$), 1453 (m), 1096 (m), 803 (m), 644 (s). HRMS (ESI, m/z): calcd for C$_{70}$H$_{73}$Fe$_2$O$_6$P$_4$ [M + H]$^+$: 1245.3051. Found: 1245.2973.

***trans*-(CO)$_3$Fe[Ph$_2$P(CH$_2$)$_6$PPh$_2$] (6′).** (BDA)Fe(CO)$_3$ (0.370 g, 1.29 mmol), Ph$_2$P(CH$_2$)$_6$PPh$_2$ (0.482 g, 1.06 mmol), and THF (14 mL) were combined in a procedure analogous to that for **4b**. An identical workup gave **6′** as a pale yellow solid (0.195 g, 0.328 mmol, 31%) that decomposed to a black solid at ≥116 °C. Anal. Calcd (%) for C$_{33}$H$_{32}$FeO$_3$P$_2$ (594.40): C, 66.68; H, 5.43. Found: C, 66.17; H, 5.64.

NMR (CDCl$_3$, δ in ppm): ^{1}H (500 MHz) 7.76 (br m, 8H, C$_6$H$_5$), 7.40 (br m, 12H, C$_6$H$_5$), 2.47 (br m, 4H, PCH$_2$), 2.06 (br m, 4H, PCH$_2$C$\underline{\boldsymbol{H}}_2$), 1.65 (br m, 4H, PCH$_2CH_2C\underline{\boldsymbol{H}}_2$). ^{13}C{^{1}H} (125 MHz)[30] 218.9 (m, 2CO), 213.2 (m, CO), 138.5 (m, i to P), 131.6 (br apparent s, o to P), 129.4 (br apparent s, p to P), 128.2 (br apparent s, m to P), 29.3 (br m, PCH$_2$), 27.3 (br m, PCH$_2\underline{\mathrm{C}}$H$_2$), 20.4 (br m, PCH$_2$CH$_2\underline{\mathrm{C}}$H$_2$). ^{31}P{^{1}H} (202 MHz) 73.13 (s). IR (powder film, cm^{-1}): 3051 (w), 2914 (w), 1965 (w, $\nu_{\mathrm{C}\equiv\mathrm{O}}$), 1863 (s, $\nu_{\mathrm{C}\equiv\mathrm{O}}$), 1433 (m), 1092 (m), 787 (m), 739 (s), 690 (s), 640 (s). HRMS (ESI, m/z): calcd for C$_{33}$H$_{32}$FeO$_3$P$_2$ [M]$^+$, 594.1176. Found 594.1164; calcd for C$_{32}$H$_{32}$FeO$_2$P$_2$ [M − CO]$^+$, 566.1227. Found 566.12119; calcd for C$_{31}$H$_{32}$FeOP$_2$ [M − 2CO]$^+$, 538.1278. Found 538.1267; calcd for C$_{30}$H$_{32}$FeP$_2$ [M − 3CO]$^+$, 510.1329. Found 510.1266.

Crystallography. *A.* A CH$_2$Cl$_2$ solution of **3** was kept at −40 °C. After 4 days, colorless blocks were collected, and data were obtained as outlined in Table 2. Cell parameters were obtained from 180 data frames taken at widths of 0.5° and refined with 9463 reflections. The unit cell was determined using the program Cell Now.[34] Integrated intensity information for each reflection was obtained by reduction of the data frames with APEX2.[35] Data were corrected for Lorentz and polarization factors, crystal decay effects, and absorption effects (using SADABS).[36] The structure was solved using SHELXTL.[37] Hydrogen atoms were placed in idealized positions and refined using a riding model. All non-hydrogen atoms were refined with anisotropic thermal parameters. Two independent molecules were found in the unit cell, each with an inversion center. Four molecules of CH_2Cl_2 were present for every molecule of **3**. Two were disordered but could be modeled successfully. However, the irregular thermal ellipsoids and residual electron density close to the chlorine atoms suggested further disorder.

B. A toluene solution of **4a** was kept at −40 °C. After 2 weeks, colorless blocks were collected, and data were obtained as outlined in Table 2. The structure was solved as in *A* (180 frames, 0.5° scan, 12 925 reflections). Two independent molecules were found in the unit cell, each with an inversion center. Six toluene molecules were present for every molecule of **4a**. Residual electron densities close to four toluene molecules indicated disorder, and each was modeled between two positions. Some of the carbon atoms exhibited irregular thermal ellipsoids, and restraints were used to keep them reasonable.

C. $CHCl_3$ vapor was allowed to slowly diffuse into a toluene solution of **4b** at 0 °C. After 2 days, yellow blocks were collected, and data were obtained as outlined in Table 2. Cell parameters were obtained from 45 data frames taken at widths of 1°. Integrated intensity information for each reflection was obtained by reduction of the data frames with APEX3.[37] All data were corrected for Lorentz and polarization factors, crystal decay effects, and (using SADABS)[36] absorption effects. The structure was solved using XT/XS in APEX3.[35,37] Solvent molecules were found. However, they were disordered, and/or the sites were partially occupied, and could not be modeled successfully. Hydrogen atoms were placed in idealized positions and refined using a riding model. All non-hydrogen atoms were refined with anisotropic thermal parameters. The solvent molecules were MASKed using OLEX2[38] during the final least-squares refinement cycles. The absence of additional symmetry and voids was confirmed using PLATON (ADDYSM).[39] The structure was refined (weighted least-squares refinement on F^2) to convergence.[37,38]

D. Pentane vapor was allowed to slowly diffuse into a toluene solution of **6′** at 0 °C. After 2 days, yellow blocks were collected, and data were obtained as outlined in Table 2. The structure was solved as in *A* (45 frames, 1° scan, 7998 reflections). A half molecule of toluene was present for every molecule of **6′**; the elongated ellipsoids suggested disorder, which was successfully modeled between two positions with a 0.66:0.34 occupancy ratio.

DFT Computations. An all-electron triple ζ quality basis set was used on all atoms including iron (def2-TZVP).[40] Thus, no pseudopotential was used on heavier elements. This basis set was paired with the TPSS[41] functional, which has been shown to reproduce experimental IR spectra of iron carbonyl complexes.[13,22] All computations were performed using the Gaussian09 program suite, employing an ultrafine grid (99 590) to enhance accuracy.[42] First, all species were optimized and then subjected to frequency calculations to perform a vibrational analysis. The IR spectra were computed for all mono- and diiron species. These calculations were separated from the optimizations, and additional memory (150 GB) was necessary to reach convergence. The vibrational frequencies were inspected and all structures were deemed to be local minima. The scaling factor (0.9863) was close to values that proved optimal in earlier studies.[43]

ASSOCIATED CONTENT

Supporting Information

The Supporting Information is available free of charge at https://pubs.acs.org/doi/10.1021/acs.inorgchem.0c03737.

Optimized geometries for computed structures (XYZ)

Additional details of the DFT computations (PDF)

Accession Codes

CCDC 2050436−2050439 contain the supplementary crystallographic data for this paper. These data can be obtained free of charge via www.ccdc.cam.ac.uk/data_request/cif, or by emailing data_request@ccdc.cam.ac.uk, or by contacting The Cambridge Crystallographic Data Centre, 12 Union Road, Cambridge CB2 1EZ, UK; fax: +44 1223 336033.

AUTHOR INFORMATION

Corresponding Authors

John A. Gladysz − *Department of Chemistry, Texas A&M University, College Station, Texas 77842-3012, United States*; orcid.org/0000-0002-7012-4872; Email: gladysz@mail.chem.tamu.edu

Michael B. Hall − *Department of Chemistry, Texas A&M University, College Station, Texas 77842-3012, United States*; orcid.org/0000-0003-3263-3219; Email: mbhall@tamu.edu

Authors

Samuel R. Zarcone − *Department of Chemistry, Texas A&M University, College Station, Texas 77842-3012, United States*

Gong M. Chu − *Department of Chemistry, Texas A&M University, College Station, Texas 77842-3012, United States*

Andreas Ehnbom − *Department of Chemistry, Texas A&M University, College Station, Texas 77842-3012, United States*; orcid.org/0000-0002-7044-1712

Ashley Cardenal − *Department of Chemistry, Texas A&M University, College Station, Texas 77842-3012, United States*; orcid.org/0000-0002-0639-8596

‡**Tobias Fiedler** − *Department of Chemistry, Texas A&M University, College Station, Texas 77842-3012, United States*

Nattamai Bhuvanesh − *Department of Chemistry, Texas A&M University, College Station, Texas 77842-3012, United States*

Complete contact information is available at: https://pubs.acs.org/10.1021/acs.inorgchem.0c03737

Notes

The authors declare no competing financial interest.
‡T.F. is deceased as of 28 October 2020.

ACKNOWLEDGMENTS

The authors thank the US National Science Foundation (J.A.G.: CHE-1566601, CHE-1900549; M.B.H.: CHE-1664866) and the Welch Foundation (M.B.H.: A-0648) for support. The authors also thank Dr. D. J. Darensbourg for helpful discussions and the Laboratory for Molecular Simulation and Texas A&M High Performance Research Computing for computational resources.

REFERENCES

(1) Kottas, G. S.; Clarke, L. I.; Horinek, D.; Michl, J. Artificial Molecular Rotors. *Chem. Rev.* **2005**, *105*, 1281−1376.

(2) Reviews of this extensive literature: (a) Iwamura, H.; Mislow, K. Stereochemical Consequences of Dynamic Gearing. *Acc. Chem. Res.* **1988**, *21*, 175−182. (b) Goswami, A.; Saha, S.; Biswas, P. K.; Schmittel, M. (Nano)mechanical Motion Triggered by Metal Coordination: from Functional Devices to Networked Multicomponent Catalytic Machinery. *Chem. Rev.* **2020**, *120*, 125−199.

(see especially section 2.2). (c) Dattler, D.; Fuks, G.; Heiser, J.; Moulin, E.; Perrot, A.; Yao, X.; Giuseppone, N. Design of Collective Motions from Synthetic Molecular Switches, Rotors, and Motors. *Chem. Rev.* **2020**, *120*, 310−433. (see especially section 4.2). (d) Liepuoniute, I.; Jellen, M. J.; Garcia-Garibay, M. A. Correlated motion and mechanical gearing in amphidynamic crystalline molecular machines. *Chem. Sci.* **2020**, *11*, 12994−13007.

(3) Some representative primary literature: (a) Frantz, D. K.; Linden, A.; Baldridge, K. K.; Siegel, J. S. Molecular Spur Gears Comprising Triptycene Rotators and Bibenzimidazole-Based Stators. *J. Am. Chem. Soc.* **2012**, *134*, 1528−1535. (b) Lemouchi, C.; Iliopoulos, K.; Zorina, L.; Simonov, S.; Wzietek, P.; Cauchy, T.; Rodríguez-Fortea, A.; Canadell, E.; Kaleta, J.; Michl, J.; Gindre, D.; Chrysos, M.; Batail, P. Crystalline Arrays of Pairs of Molecular Rotors: Correlated Motion, Rotational Barriers, and Space-Inversion Symmetry Breaking Due to Conformational Mutations. *J. Am. Chem. Soc.* **2013**, *135*, 9366−9376. (c) Pérez-Estrada, S.; Rodríguez-Molina, B.; Maverick, E. F.; Khan, S. I.; Garcia-Garibay, M. A. Throwing in a Monkey Wrench to Test and Determine Geared Motion in the Dynamics of a Crystalline One-Dimensional (1D) Columnar Rotor Array. *J. Am. Chem. Soc.* **2019**, *141*, 2413−2420.

(4) (a) de Jonge, J. J.; Ratner, M. A.; de Leeuw, S. W. Local Field Controlled Switching in a One-Dimensional Dipolar Array. *J. Phys. Chem. C* **2007**, *111*, 3770−3777. (b) Zhao, K.; Dron, P. I.; Kaleta, J.; Rogers, C. T.; Michl, J. Arrays of Dipolar Molecular Rotors in Tris(*o*-phenylenedioxy)cyclotriphosphazene. *Top. Curr. Chem.* **2014**, *354*, 163−211. (c) Sharma, K.; Friedrich, B. Pair-eigenstates and mutual alignment of coupled molecular rotors in a magnetic field. *Phys. Chem. Chem. Phys.* **2016**, *18*, 13467−13477. (d) Abolins, B. P.; Zillich, R. E.; Whaley, K. B. Quantum phases of dipolar rotors on two-dimensional lattices. *J. Chem. Phys.* **2018**, *148*, 102338.

(5) Ehnbom, A.; Gladysz, J. A. Gyroscopes and the Chemical Literature, 2002−2020: Approaches to a Nascent Family of Molecular Devices. *Chem. Rev.* **2021**, DOI: 10.1021/acs.chemrev.0c01001.

(6) Lead references, square planar complexes: (a) Nawara-Hultzsch, A. J.; Stollenz, M.; Barbasiewicz, M.; Szafert, S.; Lis, T.; Hampel, F.; Bhuvanesh, N.; Gladysz, J. A. Gyroscope-Like Molecules Consisting of PdX_2/PtX_2Rotators within Three-Spoke Dibridgehead Diphosphine Stators: Syntheses, Substitution Reactions, Structures, and Dynamic Properties. *Chem. - Eur. J.* **2014**, *20*, 4617−4637. (b) Kharel, S.; Joshi, H.; Bhuvanesh, N.; Gladysz, J. A. Syntheses, Structures, and Thermal Properties of Gyroscope-like Complexes Consisting of $PtCl_2$ Rotators Encased in Macrocyclic Dibridgehead Diphosphines $P((CH_2)_n)_3P$ with Extended Methylene Chains ($n = 20/22/30$) and Isomers Thereof. *Organometallics* **2018**, *37*, 2991−3000. (c) Estrada, A. L.; Jia, T.; Bhuvanesh, N.; Blümel, J.; Gladysz, J. A. Substitution and Catalytic Chemistry of Gyroscope-Like Complexes Derived from Cl−Rh−CO Rotators and Triply *trans* Spanning Di(trialkylphosphine) Ligands. *Eur. J. Inorg. Chem.* **2015**, *2015*, 5318−5321.

(7) Lead references, trigonal bipyramidal complexes: (a) Lang, G. M.; Shima, T.; Wang, L.; Cluff, K. J.; Skopek, K.; Hampel, F.; Blümel, J.; Gladysz, J. A. Gyroscope-Like Complexes Based on Dibridgehead Diphosphine Cages That Are Accessed by Three-Fold Intramolecular Ring Closing Metatheses and Encase $Fe(CO)_3$, $Fe(CO)_2(NO)^+$, and $Fe(CO)_3(H)^+$ Rotators. *J. Am. Chem. Soc.* **2016**, *138*, 7649−7663. (b) Lang, G. M.; Skaper, D.; Hampel, F.; Gladysz, J. A. Synthesis, reactivity, structures, and dynamic properties of gyroscope like iron complexes with dibridgehead diphosphine cages: pre- *vs.* post-metathesis substitutions as routes to adducts with neutral dipolar Fe(CO)(NO)(X) rotors. *Dalton Trans.* **2016**, *45*, 16190−16204.

(8) Lead references, octahedral complexes: (a) Fiedler, T.; Bhuvanesh, N.; Hampel, F.; Reibenspies, J. H.; Gladysz, J. A. Gyroscope like molecules consisting of trigonal or square planar osmium rotators within three-spoked dibridgehead diphosphine stators: syntheses, substitution reactions, structures, and dynamic properties. *Dalton Trans.* **2016**, *45*, 7131−7147. (b) Hess, G. D.; Fiedler, T.; Hampel, F.; Gladysz, J. A. Octahedral Gyroscope-like Molecules Consisting of Rhenium Rotators within Cage-like Dibridgehead Diphosphine Stators: Syntheses, Substitution Reactions, Structures, and Dynamic Properties. *Inorg. Chem.* **2017**, *56*, 7454−7469.

(9) Syntheses and crystal structures of *cis*-$(CO)_3Fe[Ph_2P(CH_2)_5PPh_2]$ (**5′**) and *trans,trans*-$(CO)_3Fe[Ph_2P(CH_2)_5PPh_2]_2Fe(CO)_3$ (**5**): Liu, L.-K.; Luh, L.-S.; Gau, H.-M. Preparation and Structure Studies of Monomeric and Dimeric [Bis(diphenylphosphino)pentane]tricarbonyliron(0). *Inorg. Chem.* **1992**, *31*, 3434−3437.

(10) Crystal structure of *cis*-$(CO)_3Fe[Ph_2PCH_2PPh_2]$ (**1′**): Cotton, F. A.; Hardcastle, K. I.; Rusholme, G. A. An X-ray Structural Study of the Fluxional Molecule [bis(diphenylphosphino)methane]-tricarbonyliron. *J. Coord. Chem.* **1973**, *2*, 217−223.

(11) The energies of trigonal bipyramidal and square planar isomers can be quite close, with modest intervening barriers, and intermediate structures are sometimes found.[10,12] To help differentiate borderline cases, a "tau" parameter has been devised: Crans, D. C.; Tarlton, M. L.; McLauchlan, C. C. Trigonal Bipyramidal or Square Pyramidal Coordination Geometry? Investigating the Most Potent Geometry for Vanadium Phosphatase Inhibitors. *Eur. J. Inorg. Chem.* **2014**, *2014*, 4450−4468. and earlier papers cited therein; 1 = tbp, 0 = sq pyr. Those associated with **1′**, **2′**, **3′**, **5′**, and **6′** are 0.76, 0.33, 0.93, 0.74, and 0.10, respectively. Those for the diiron complexes range from 0.92 to 0.84.

(12) Synthesis and crystal structure of *cis*-$(CO)_3Fe[Ph_2P(CH_2)_2PPh_2]$ (**2′**): Battaglia, L. P.; Delledonne, D.; Nardelli, M.; Pelizzi, C.; Predieri, G.; Chiusoli, G. P. The crystal and molecular structure of [bis(diphenylphosphino) ethane] tricarbonyliron(0). *J. Organomet. Chem.* **1987**, *330*, 101−113.

(13) Synthesis and crystal structure of *cis*-$(CO)_3Fe[Ph_2P(CH_2)_3PPh_2]$ (**3′**): Ringenberg, M. R.; Wittkamp, F.; Apfel, U.-P.; Kaim, W. Redox Induced Configurational Isomerization of Bisphosphine-Tricarbonyliron(I) Complexes and the Difference a Ferrocene Makes. *Inorg. Chem.* **2017**, *56*, 7501−7511.

(14) Other works reporting syntheses of *cis*-$(CO)_3Fe[Ph_2P(CH_2)_nPPh_2]$: (a) $n = 1$ (**1′**): Wegner, P. A.; Evans, L. F.; Haddock, J. Bimetallic Iron Carbonyl Derivatives of Bidentate Phosphine Ligands. *Inorg. Chem.* **1975**, *14*, 192−194. (b) $n = 1$−4 (**1′**−**4′**): Sowa, J. R. Jr.; Zanotti, V.; Facchin, G.; Angelici, R. J. Calorimetric Studies of the Heats of Protonation of the Metal in $Fe(CO)_3$(bidentate phosphine, arsine) Complexes: Effects of Chelate Ligands on Metal Basicity. *J. Am. Chem. Soc.* **1992**, *114*, 160−165. (c) $n = 1$−4 (**1′**−**4′**): Luo, L.; Nolan, S. P. Enthalpies of Reaction of (Diene)- and (Enone)iron Tricarbonyl Complexes with Monodentate and Bidentate Ligands. Solution Thermochemical Study of Ligand Substitution in the $L_2Fe(CO)_3$ Complexes. *Inorg. Chem.* **1993**, *32*, 2410−2415. (d) $n = 3$ (**3′**): Langford, G. R.; Akhtar, M.; Ellis, P. D.; MacDiarmid, A. G.; Odom, J. D. Synthesis and Multinuclear Magnetic Resonance Study of Stereochemically Nonrigid Derivatives of Iron Pentacarbonyl Containing Bidentate Ligands. *Inorg. Chem.* **1975**, *14*, 2937−2941.

(15) (a) Howell, J. A. S.; Johnson, B. F. G.; Josty, P. L.; Lewis, J. Synthesis and reactions of tetracarbonyl- and tricarbonyliron complexes of *α,β*-unsaturated ketones. *J. Organomet. Chem.* **1972**, *39*, 329−333. (b) Brookhart, M.; Nelson, G. O. The reaction of benzylideneacetoneiron tricarbonyl with dienes; measurement of relative reactivities using competition experiments. *J. Organomet. Chem.* **1979**, *164*, 193−202.

(16) (a) Skopek, K.; Gladysz, J. A. Syntheses of gyroscope-like molecules via three-fold ring closing metatheses of bis(phosphine) complexes *trans*-$L_yM(P((CH_2)_nCH{=}CH_2)_3)_2$, and extensions to bis(phosphite) complexes *trans*-$Fe(CO)_3(P(O(CH_2)_nCH{=}CH_2)_3)_2$. *J. Organomet. Chem.* **2008**, *693*, 857−866. (b) Lang, G. M.; Skaper, D.; Shima, T.; Otto, M.; Wang, L.; Gladysz, J. A. Syntheses of Iron(0) Complexes of Symmetrical Trialkylphosphines with Three Terminal Vinyl Groups, $P((CH_2)_mCH{=}CH_2)_3$. *Aust. J. Chem.* **2015**, *68*, 1342−1351. (c) Steigleder, E.; Shima, T.; Lang, G. M.; Ehnbom, A.;

Hampel, F.; Gladysz, J. A. Partially Shielded $Fe(CO)_3$ Rotors: Syntheses, Structures, and Dynamic Properties of Complexes with Doubly *trans* Spanning Diphosphines, *trans*-$Fe(CO)_3(PhP((CH_2)_n)_2PPh)$. *Organometallics* **2017**, *36*, 2891−2901.

(17) Leitner, W.; Bühl, M.; Fornika, R.; Six, C.; Baumann, W.; Dinjus, E.; Kessler, M.; Krüger, C.; Rufińska, A. ^{103}Rh Chemical Shifts in Complexes Bearing Chelating Bidentate Phosphine Ligands. *Organometallics* **1999**, *18*, 1196−1206.

(18) Adams, D. M. Metal−Ligand and Related Vibrations. St. Martin's Press: New York, 1968; Chapter 3.4.

(19) The IR spectrum of **4a** (Figure 1) exhibits some weak features that do not have counterparts in the spectra of **3** or **4b**. These do not arise from any **4′a** contaminant.

(20) Throughout this manuscript, primed compound numbers indicate monoiron complexes $(CO)_3Fe[Ph_2P(CH_2)_nPPh_2]$ regardless of coordination geometry or stereochemistry. All trigonal bipyramidal complexes presented have *cis* phosphorus donor atoms (**3′**, **4′a**, **5′**; axial/equatorial), but square pyramidal complexes can be either *cis* (**1′**, **2′**) or *trans* (**6′**, **6′′**; basal/basal in all cases).

(21) (a) Bondi, A. van der Waals Volumes and Radii. *J. Phys. Chem.* **1964**, *68*, 441−451. (b) Mantina, M.; Chamberlin, A. C.; Valero, R.; Cramer, C. J.; Truhlar, D. G. Consistent van der Waals Radii for the Whole Main Group. *J. Phys. Chem. A* **2009**, *113*, 5806−5812.

(22) Representative studies validating the use of the TPSS functional and/or def2-TZVP basis set for IR calculations in related systems: (a) Brothers, S. M.; Darensbourg, M. Y.; Hall, M. B. Modeling Structures and Vibrational Frequencies for Dinitrosyl Iron Complexes (DNICs) with Density Functional Theory. *Inorg. Chem.* **2011**, *50*, 8532−8540. (b) Meng, L.; Liu, S.; Qin, Q.; Zeng, B.; Chi, C. Infrared Photodissociation Spectroscopy of Heteronuclear Arsenic-Iron Carbonyl Cluster Anions. *J. Phys. Chem. A* **2020**, *124*, 1158−1166. (c) Speelman, A. L.; Zhang, B.; Silakov, A.; Skodje, K. M.; Alp, E. E.; Zhao, J.; Hu, M. Y.; Kim, E.; Krebs, C.; Lehnert, N. Unusual Synthetic Pathway for an $\{Fe(NO)_2\}^9$ Dinitrosyl Iron Complex (DNIC) and Insight into DNIC Electronic Structure via Nuclear Resonance Vibrational Spectroscopy. *Inorg. Chem.* **2016**, *55*, 5485−5501. (d) Pan, S.; Zhao, L.; Dias, H. V. R.; Frenking, G. Bonding in Binuclear Carbonyl Complexes $M_2(CO)_9$ (M = Fe, Ru, Os). *Inorg. Chem.* **2018**, *57*, 7780−7791. (e) Kerpal, C.; Harding, D. J.; Rayner, D. M.; Fielicke, A. Small Platinum Cluster Hydrides in the Gas Phase. *J. Phys. Chem. A* **2013**, *117*, 8230−8237.

(23) Bessel, C. A.; Aggarwal, P.; Marschilok, A. C.; Takeuchi, K. J. Transition-Metal Complexes Containing *trans*-Spanning Diphosphine Ligands. *Chem. Rev.* **2001**, *101*, 1031−1066.

(24) A report of a square planar nickel complex with a *trans*-spanning pentamethylene diphosphine $Cy_2P(CH_2)_5PCy_2$ has been questioned:[23] Issleib, V. K.; Hohlfeld, G. Beiträge zur Komplexchemie der Phosphine und Phosphinoxyde. X. Schwermetallkomplexe ditertiärer Phosphine. *Z. Anorg. Allg. Chem.* **1961**, *312*, 169−179.

(25) Casey, C. P.; Whiteker, G. T.; Campana, C. F.; Powell, D. R. Pentacoordinate $Fe(CO)_3$ Complexes of Diphosphine Ligands with Bite Angles Greater Than 120°. *Inorg. Chem.* **1990**, *29*, 3376−3381.

(26) See the following lead references, and earlier work cited therein: (a) Balch, A. L.; Tulyathan, B. Interactions between rhodium(I) centers in dimeric complexes. *Inorg. Chem.* **1977**, *16*, 2840−2845. (b) Cowie, M.; Dwight, S. K. Unusual structural and chemical trends within a series of binuclear rhodium carbonyl halide complexes and the structure of one member of this series, *trans*-$[Rh_2Cl_2(CO)_2((C_6H_5)_2PCH_2P(C_6H_5)_2)_2]$. *Inorg. Chem.* **1980**, *19*, 2500−2507.

(27) Cecconi, F.; Midollini, S.; Orlandini, A.; Sacconi, L. Trimeric nickel(II) complexes with bridging triphosphine ligand 1,1,1-tris(diphenylphosphinoethyl)ethane (etp$_3$). X-ray structure of the complex $[Ni_3Cl_6(etp_3)_2]\cdot 0.7CHCl_3$. *Inorg. Chim. Acta* **1980**, *42*, 59−63.

(28) Jiang, X.; Xiao, Z.; Zhong, W.; Liu, X. Brief survey of diiron and monoiron carbonyl complexes and their potentials as CO-releasing molecules (CORMs). *Coord. Chem. Rev.* **2021**, *429*, No. 213634.

(29) The ^{1}H and ^{13}C{^{1}H} NMR signal assignments are made by analogy to those rigorously verified for $(p\text{-tol})_2P(CH_2)_{14}P(p\text{-tol})_2$ earlier. See de Quadras, L.; Stahl, J.; Zhuravlev, F.; Gladysz, J. A. Monophosphine and diphosphine ligands for diplatinum polyynediyl complexes: Efficient syntheses of new functionality-containing systems and model compounds. *J. Organomet. Chem.* **2007**, *692*, 1859−1870. and endnote 27 therein.

(30) Of the phenyl ^{13}C{^{1}H} NMR signals, that with the chemical shift closest to benzene (128.4 ppm) is attributed to the *meta* carbon atom, and the other signal of comparable intensity (and phosphorus coupling) is attributed to the *ortho* carbon atom. See Mann, B. E. The Carbon-13 and Phosphorus-31 Nuclear Magnetic Resonance Spectra of Some Tertiary Phosphines. *J. Chem. Soc., Perkin Trans. 2* **1972**, 30−34.

(31) The ^{31}P{^{1}H} NMR spectra of the crude reaction mixture suggest that some **4′a**[14b] may be formed. However, this species is removed upon workup.

(32) For virtual triplets, the $^xJ_{CP}$ values represent *apparent* couplings between adjacent peaks that take place through a minimum of *x* bonds. Hersh, W. H. False AA′X Spin-Spin Coupling Systems in ^{13}C NMR: Examples Involving Phosphorus and a 20-Year-Old Mystery in Off-Resonance Decoupling. *J. Chem. Educ.* **1997**, *74*, 1485−1488.

(33) All reported syntheses have been carried out by at least two co-workers. In this case, the second found that pure **4b** was best obtained by scaling down the solvent volume (THF, 3.3 mL; $(BDA)Fe(CO)_3$, 0.200 g/0.414 mmol; $(p\text{-tol})_2P(CH_2)_4P(p\text{-tol})_2$, 0.145 g/0.506 mmol). Otherwise what was presumed to be **4′b** (based upon the chemical shift relationship exhibited by **5′** and **5**)[9] dominated after workup.

(34) Sheldrick, G. M. *Cell_Now: Program for Obtaining Unit Cell Constants from Single Crystal Data*, version 2008/1; University of Göttingen, 2007.

(35) *APEX2/3*; Bruker AXS Inc.: Madison, WI, 2016.

(36) Sheldrick, G. M. *SADABS*; Bruker AXS Inc.: Madison, WI, 2001.

(37) (a) Sheldrick, G. M. A short history of SHELX. *Acta Crystallogr., Sect. A: Found. Crystallogr.* **2008**, *A64*, 112−122. (b) Sheldrick, G. M. SHELXT − Integrated space-group and crystal structure determination. *Acta Crystallogr., Sect. A: Found. Adv.* **2015**, *71*, 3−8. (c) Sheldrick, G. M. Crystal structure refinement with SHELXL. *Acta Crystallogr., Sect. C: Struct. Chem.* **2015**, *C71*, 3−8. (d) *XT, XS*; Bruker AXS Inc.: Madison, WI, 2016.

(38) Dolomanov, O. V.; Bourhis, L. J.; Gildea, R. J.; Howard, J. A. K.; Puschmann, H. OLEX2: A Complete Structure Solution, Refinement and Analysis Program. *J. Appl. Crystallogr.* **2009**, *42*, 339−341.

(39) Spek, A. L. Single-crystal structure validation with the program. *J. Appl. Crystallogr.* **2003**, *36*, 7−13.

(40) Weigend, F.; Ahlrichs, R. Balanced basis sets of split valence, triple zeta valence and quadruple zeta valence quality for H to Rn: Design and assessment of accuracy. *Phys. Chem. Chem. Phys.* **2005**, *7*, 3297−3305.

(41) Tao, J.; Perdew, J. P.; Staroverov, V. N.; Scuseria, G. E. Climbing the Density Functional Ladder: Nonempirical Meta-Generalized Gradient Approximation Designed for Molecules and Solids. *Phys. Rev. Lett.* **2003**, *91*, 146401.

(42) Frisch, M. J.; Trucks, G. W.; Schlegel, H. B.; Scuseria, G. E.; Robb, M. A.; Cheeseman, J. R.; Scalmani, G.; Barone, V.; Mennucci, B.; Petersson, G. A.; Nakatsuji, H.; Caricato, M.; Li, X.; Hratchian, H. P.; Izmaylov, A. F.; Bloino, J.; Zheng, G.; Sonnenberg, J. L.; Hada, M.; Ehara, M.; Toyota, K.; Fukuda, R.; Hasegawa, J.; Ishida, M.; Nakajima, T.; Honda, Y.; Kitao, O.; Nakai, H.; Vreven, T.; Montgomery, J. A., Jr.; Peralta, J. E.; Ogliaro, F.; Bearpark, M.; Heyd, J. J.; Brothers, E.; Kudin, K. N.; Staroverov, V. N.; Kobayashi, R.; Normand, J.; Raghavachari, K.; Rendell, A.; Burant, J. C.; Iyengar, S. S.; Tomasi, J.; Cossi, M.; Rega, N.; Millam, J. M.; Klene, M.; Knox, J. E.; Cross, J. B.; Bakken, V.; Adamo, C.; Jaramillo, J.; Gomperts, R.; Stratmann, R. E.; Yazyev, O.; Austin, A. J.; Cammi, R.; Pomelli, C.; Ochterski, J. W.; Martin, R. L.; Morokuma, K.; Zakrzewski, V. G.;

Voth, G. A.; Salvador, P.; Dannenberg, J. J.; Dapprich, S.; Daniels, A. D.; Farkas, Ö.; Foresman, J. B.; Ortiz, J. V.; Cioslowski, J.; Fox, D. J. *Gaussian 09*, revision D.01; Gaussian, Inc.: Wallingford, CT, 2009.

(43) (a) Kesharwani, M. K.; Brauer, B.; Martin, J. M. L. Frequency and Zero-Point Vibrational Energy Scale Factors for Double-Hybrid Density Functionals (and Other Selected Methods): Can Anharmonic Force Fields Be Avoided? *J. Phys. Chem. A* **2015**, *119*, 1701−1714. (b) Assefa, M. K.; Devera, J. L.; Brathwaite, A. D.; Mosley, J. D.; Duncan, M. A. Vibrational scaling factors for transition metal carbonyls. *Chem. Phys. Lett.* **2015**, *640*, 175−179.